Fall 12-11-2023

Studies of Attosecond Time Delay and Superheavy Elements in Atomic Photoionization

Rezvan Khademhosseini
Georgia State University

Studies of Attosecond Time Delay and Superheavy Elements in Atomic Photoionization

by

Rezvan Khademhosseini

Under the Direction of Steven T. Manson, PhD

A Dissertation Submitted in Partial Fulfillment of the Requirements for the Degree of

Doctor of philosophy

in the College of Arts and Sciences

Georgia State University

2023

ABSTRACT

This research consists of two distinct but related elements in the realm of atomic photoionization. The first was to explore the photoionization in superheavy elements. Employing the fully Relativistic Random Phase Approximation (RRPA), we calculated the photoionization cross sections for the Oganesson (Og), the heaviest element, since the influence of relativity becomes more significant as the atomic number increases. The results revealed the importance of relativistic interactions along with the predominant influence of interchannel coupling on the photoionization cross sections. Encouraged by the ability of the RRPA to deal with the combination of relativistic and many-body correlation effects, we proceeded to investigate the angle-dependent time delay in the photoionization process using the RRPA. Specifically, we investigated the time delay in argon. The matrix elements calculated using RRPA were used to calculate the phases of the various photoionization amplitudes, and the energy derivative of these phases provided us with the time delay information. We computed a weighted average of the time delays associated with dipole and quadrupole components, averaged over photoelectron spin and orientation of the residual ion, considering different transitions involved in the photoionization process. Time delay in photoionization exhibits angular dependence, a phenomenon explored in previous calculations considering only dipole transitions. In the nonrelativistic dipole approximation, time delay for atomic ns-states is angle-independent. However, incorporating relativistic effects, such as spin-flip transitions and non-dipole (quadrupole) effects, introduces angular dependence to the time delay. This is especially prominent when dominant dipole photoionization channels (without spin-flip) vanish at specific angles due to angular momentum geometry. In these instances, quadrupole and spin-flip transitions dominate. When the dipole amplitude vanishes, time delay results from a combination of spin-flip dipole and quadrupole time

delays. Relativistic expressions have been formulated to delineate the conditions where quadrupole and/or spin-flip channels influence the time delay. We focus on the 3s subshell in argon to highlight the complex effects of spin-flip and quadrupole transitions. Of particular interest is the presence of a significant Cooper minimum in the cross section, leading to notably long time delays. Our goal is to explore these dynamics and understand the intricate processes in photoionization.

INDEX WORDS: Photoionization, Time delay, Superheavy elements

Studies of Attosecond Time Delay and Superheavy Elements in Atomic Photoionization

by

Rezvan Khademhosseini

Committee Chair: Steven T. Manson

Committee: Megan Elizabeth Connors

Vadym Apalkov

Sidong Lei

Electronic Version Approved:

Office of Graduate Services

College of Arts and Sciences

Georgia State University

December 2023

DEDICATION

This dissertation is dedicated to my parents, my husband, and my son. You are the foundation of my world, the source of my strength, and the reason behind every step of this academic journey. Through your unwavering support, endless patience, and boundless love, you have made it possible for me to pursue this path of knowledge. This achievement would not have been possible without your love and support. Thank you for being the pillars of strength in my life.

ACKNOWLEDGEMENTS

I am deeply grateful for the invaluable guidance and support provided by my advisor, Dr. Steven T. Manson, throughout my research journey. His expertise, encouragement, and steadfast dedication to my academic growth have been crucial in shaping this dissertation. I extend my heartfelt appreciation to Dr. Pranawa C. Deshmukh and Ms. Chathuranga Rasadi Munasinghe, as members of my research group, for their collaborative spirit, insightful discussions, and shared passion for our research endeavors. I would like to express my sincere thanks to my committee members, Dr. Megan Elizabeth Connors, Dr. Vadym Apalkov, and Dr. Sidong Lei, for their valuable feedback, and expert guidance. Their collective expertise and diverse perspectives have immensely enriched the quality of this research. My heartfelt gratitude also goes to all the staff and colleagues who have contributed to this academic endeavor, directly or indirectly. Your support made this challenging journey not only intellectually stimulating but also deeply rewarding. Thank you all for your enduring support and belief in my work. I am truly fortunate to have had such a dedicated and inspiring team to accompany me on this scholarly pursuit.

TABLE OF CONTENTS

LIST OF TABLES

LIST OF FIGURES

LIST OF ABBREVIATIONS

RRPA – Relativistic Random Phase Approximation

RPA - Random Phase Approximation

DF - Dirac-Fock

a.u. – Atomic units

Ar – Argon

Og - Oganesson

SOIAIC - Spin Orbit Interaction Activated Interchannel Coupling

XUV - Extreme Ultraviolet

CLC – Coulomb Laser Coupling

WES - Wigner Eisenberg Smith

as – Attosecond

eV – Electron Volts

1 INTRODUCTION

The realm of atomic photoionization is a captivating arena where the fundamental properties of atoms and molecules are probed through their interactions with photons. Within this domain, two remarkable frontiers have emerged, each offering unique insights into the behavior of matter at the atomic and subatomic levels. This dissertation explores these frontiers, focusing on the phenomena of attosecond time delay and the intriguing world of superheavy elements in the context of atomic photoionization. Attosecond physics, an area of study where we delve into time intervals as short as 10^{-18}seconds, has enshanced our understanding of how electrons move within atoms. Simultaneously, we venture into the realm of superheavy elements, which are elements with atomic numbers exceeding 103. These elements reside at the edge of the periodic table and exhibit unique properties due to their extremely relativistic nature. Investigating the photoionization and structural properties of superheavy elements like Oganesson (Og, Z=118) forms a central part of our research. Superheavy elements, unlike their counterparts at the low end of the Periodic Table, are uniquely influenced by the combined effects of relativistic and correlation factors. These two factors play a critical role in understanding the fundamental properties of superheavy elements, making their study distinct from lighter elements [1]. Due to the significant strength of relativistic effects, especially in heavy and superheavy elements, theoretical models must be based on the Dirac equation, which accounts for relativistic corrections, rather than the non-relativistic Schrödinger equation. In this context, the focus of the study is on the photoionization process of the ground states of these superheavy atoms, and researchers are employing the relativistic-random-phase approximation (RRPA) [23,25] to explore this phenomenon. Relativistic effects become increasingly important as the atomic number (Z) of elements increases. For superheavy atoms, where Z is extremely high, these effects cannot be

neglected. Relativistic corrections to the electronic structure and behavior of electrons within the atom are substantial and need to be accurately accounted for in theoretical calculations. For heavy and superheavy atoms, calculations based on the Dirac equation [2,3] are essential to accurately model the electronic structure and interactions. RRPA is an advanced theoretical method used to study the excited states of atomic and molecular systems in the presence of relativistic effects and many-body electron-electron correlations. By employing RRPA, researchers can explore the interplay between relativistic effects and the complex electron-electron interactions within superheavy atoms. This approach allows for a detailed investigation of processes like photoionization, shedding light on the behavior of electrons in these extreme atomic environments. In the framework of the relativistic random-phase approximation (RRPA), electron transitions resulting from photoionization are described using complex dipole matrix elements [4]. This complexity in the photoionization matrix element is a fundamental aspect of the RRPA model. In a transition from an initial bound state to a continuum state the dipole matrix element is inherently complex. This complexity is vital for accurately describing the intricate quantum interactions involved in the photoionization process. The derivative of the phase of this complex matrix element with respect to energy, denoted as $d\delta(E)/dE$, serves as a measure of the time delay occurring in various dipole photoionization channels. This derivative quantity provides valuable information about the temporal aspects of the photoionization process, allowing researchers to analyze the subtle delays in the release of the photoelectron wave packet after the absorption of a brief electromagnetic pulse. Time delay in atomic photoionization indeed refers to the minor temporal delay that is observed in the release of the photoelectron wave packet following the absorption of a short electromagnetic pulse. This phenomenon provides valuable insights into the intricate dynamics of electron behavior at the quantum level and is a crucial concept in the study

of ultrafast processes in atomic and molecular physics. The interest in attosecond time delay in atomic and molecular photoionization was sparked by precise experimental measurements at the attosecond level [5]. Researchers were captivated by the opportunity to understand the behavior of electrons during transitions within atoms and molecules on an incredibly fast timescale. This curiosity led to numerous experimental and theoretical investigations [6] aimed at unraveling the complexities of attosecond time delay in atomic and molecular photoionization processes. Researchers have achieved remarkable precision in measuring the relative time delay of photoemission between neighboring valence atomic subshells, specifically in the context of argon [7,8]. Research interest in the time delay has surged due to pioneering experiments by various researchers [9]. Subsequent studies [10] have primarily focused on the valence electron shells of noble gas atoms. Relativistic random phase approximation (RRPA) calculations for the angular dependence of time delay of s-subshells of noble gas atoms for the angular distribution of time delay including both dipole and quadrupole channels have been performed as a function of the angle between the photoelectron momentum and photon polarization and the transition from dipole to quadrupole time delay is exhibited in the present work.

2 THEORY

2.1 Photoionization

Photoionization is a process in which an atom or molecule absorbs a photon with enough energy to remove an electron from its atomic or molecular orbital, leading to a positively charged ion. The probability of photoionization depends on the energy of the photon and the ionization energy of the atom or molecule. The initial investigations into photoionization were performed in the 1920s [11], primarily focusing on the alkali metals since the ionization potentials of these metals fall within the wavelength range of 2000 to 3000 Å. This spectral region provided a convenient and straightforward range for conducting the measurements [12]. Photoionization is the phenomenon in which an atom or molecule in state i is ionized by the absorption of a photon with energy hν, resulting in the formation of a positively charged ion in state j. Here, the atom or molecule is denoted as $X(i)$, and the ion as $X(j)^+$:

$$h\nu + X(i) \rightarrow X(j)^+ + e^- \quad (2.1)$$

and the relation for the energies is:

$$\varepsilon = h\nu - I_{ij} \quad (2.2)$$

where, ε represents the kinetic energy of the emitted photoelectron, $h\nu$ is the energy of the photon, and I_{ij} refers to the minimum energy required to remove an electron from the atom, leaving behind the ion. This energy is commonly known as the binding energy of the electron [13].

2.1.1 The interaction Hamiltonian

The Hamiltonian for an N-electron atom with nuclear charge Z in the nonrelativistic approximation is described by:

$$H = \sum_{i=1}^{N}\left(\frac{p_i^2}{2m} - \frac{Ze^2}{r_i}\right) + \sum_{i>j=1}^{N}\frac{e^2}{|r_i - r_j|} \ , \qquad p = -i\hbar\nabla. \tag{2.3}$$

The first term describes the kinetic and potential energy in the attractive Coulomb field generated by the nucleus, m is the particle mass, p is the momentum operator, Z represents the nuclear charge, e is the electron charge, and r_i is the distance between the i-th electron and the nucleus. This term represents the attractive interaction between the negatively charged electrons and the positively charged nucleus. The last term describes the repulsive electrostatic potential energy between the i-th electron and the j-th electron, and depends on the inverse of the distance between them. The interaction between this atom and external electromagnetic radiation is explained by incorporating additional terms obtained by substituting p_i by $p_i + \left({}^{|e|}/_{c}\right)A(r_i, t)$ where $A(r_i, t)$ is the vector potential for the radiation. The interaction Hamiltonian is:

$$H_{int} = \sum_{i=1}^{N}\left\{\frac{+|e|}{2mc}[p_i \,.A(r_i, t) + A(r_i, t).\, p_i] + \frac{|e|^2}{2mc^2}|A(r_i, t)|^2\right\} \tag{2.4}$$

where $A(r_i, t)$ is the vector potential for the radiation. Simplifying the interaction Hamiltonian, as outlined in equation (2.4) can make dealing with the ionization of a single photon and an electron from an outer-subshell much easier. We can achieve this by disregarding the third term in the equation (2.4), which is related to processes that involve the absorption of two photons. Further, this term is second order in the (small) vector potential A and is insignificant when compared to single-photon processes. The impact of this term would be relatively small as it is second-order in the coupling constant |e|/c, resulting in a negligible effect on the ionization process [14]. Additionally, in our approach, we adopt the Coulomb gauge for the vector potential A, where we set the $\nabla \cdot A = 0$. The Coulomb gauge formalism offers a significant advantage in physics due to the instantaneous electrostatic interaction between charges. However, it is important to note that in higher-order calculations involving point charges or situations where atoms or molecules

interact with radiation, the conventional Coulomb gauge formalism can introduce certain ambiguities [15]. The variable A represents a transverse radiation field. Additionally, it is noteworthy that p and A now have commutative properties, allowing us to combine the first and second terms in equation (2.4):

If we consider $\vec{p} = -i\hbar\vec{\nabla}$, operating on an arbitrary function F:

$$\{(\vec{\nabla}.\vec{A}(r_i,t) + \vec{A}(r_i,t).\vec{\nabla})\}F = \vec{\nabla}.(\vec{A}(r_i,t)F) + \vec{A}(r_i,t).\vec{\nabla}F =$$

$$\left(\vec{\nabla}.\vec{A}(r_i,t)\right)F + \vec{A}(r_i,t).\vec{\nabla}F + \vec{A}(r_i,t).\vec{\nabla}F = 2\,\vec{A}(r_i,t).\vec{\nabla}F \quad (2.5)$$

The first term vanishes but the two remaining terms add up. And this will be the perturbation, the interaction Hamiltonian. To proceed further, we introduce a specific form for A as follows:

$$A(r_i,t) = \left(\frac{2\pi c^2\hbar}{\omega V}\right)^{1/2} \hat{\epsilon} e^{i(k.r_i-\omega t)} \quad (2.6)$$

where V is the spatial volume, $\hat{\epsilon}$ is the polarization unit vector, k and ω are the wave vector and angular frequency of the incident radiation. This classical expression for A is capable of accurately predicting photoabsorption transition rates. Remarkably, these rates are found to be in agreement with those obtained through the quantum theory of radiation. This significant finding further establishes the harmony between classical and quantum frameworks when it comes to comprehending and explaining photoabsorption phenomena [16]. Using the electric dipole approximation, which is a commonly used technique in physics, the term $e^{i(k.r_i)}$ is simplified to unity. While the electric dipole approximation is often suitable for many cases, it should not be applied without critical evaluation. Certain scenarios challenge its validity. For instance, photoionization of excited atoms with larger radii, photoionization of inner subshells requiring short wavelength radiation, and calculations involving differential cross sections or other measurable quantities that rely on the overlap of electric dipole and higher multipole amplitudes

all demand careful scrutiny of the electric dipole approximation. In such situations, it becomes necessary to assess the validity and potential limitations of the electric dipole approximation before relying on its application. Therefore, expanding the vector potential A in terms of position vector r yields a series of multipole moments of increasing order, keeping only the lowest-order term provides a good approximation [17]:

$$exp\left(\pm i(k.r-\omega t)\right) = exp\left(\pm 2\pi i \frac{|r|}{\lambda}\hat{k}.\hat{r}\right)e^{\mp i\omega t} \approx \left(1+\mathcal{O}\left(\frac{|r|}{\lambda}\right)\right)e^{\mp i\omega t} \quad (2.7)$$

In order to simplify the equation (2.4) by truncating the Taylor expansion (equation 2.7) to just the first term assuming that $|\vec{r}| \ll {}^{\lambda}/_{2\pi}$, where λ is the wavelength. Upon applying these conventions and approximations and substituting the relevant equations, the resulting expression for the interaction Hamiltonian is as follows:

$$H_{int} = \frac{+|e|}{mc}\left(\frac{2\pi c^2\hbar}{\omega V}\right)^{1/2}\sum_{i=1}^{N}\hat{\epsilon}.p_i\, e^{-i\omega t} \quad (2.8)$$

H_{int} thus has the form of a harmonically time-dependent perturbation. Within perturbation theory, the interaction Hamiltonian is expanded in terms of the perturbation parameter, which represents the strength of the interaction. The expansion allows us to analyze the effects of the external radiation on the atomic or molecular system and calculate the photoionization cross section. The photoionization cross section is a measure of the probability of ionization and is obtained by evaluating the matrix elements of the interaction Hamiltonian between the initial and final states of the system. By employing perturbation theory and calculating the matrix elements of the interaction Hamiltonian, we can quantitatively study the photoionization process and understand the dynamics of ionization. This approach enables us to investigate how the incident radiation interacts with the atomic or molecular system and provides valuable insights into the underlying physics of photoionization phenomena.

The probability of photoionizing an atom by an incident photon of energy $\hbar\omega$ is represented by the cross section of the system. This cross section provides valuable information about the system's interaction with the radiation. The transition probability, denoted as P_{if} in Equation (2.9), describes the probability per unit time for a transition to take place between the initial state i and the final state f:

$$P_{if} = \frac{2\pi}{\hbar}\left|\langle\Psi_f|\hat{H}_{int}|\Psi_i\rangle\right|^2\delta(E_f - E_i - \hbar\omega) \tag{2.9}$$

where $|\Psi_i\rangle$ and $|\Psi_f\rangle$ represents the initial state and final state wave functions and the squared matrix elements give the transition rate. E_i is the energy of the initial state and E_f is the energy of the final state. The Dirac function δ represents energy conservation, indicating that a transition occurs when $E_f = E_i + \hbar\omega$. This probability is determined using Fermi's golden rule, which is a fundamental principle derived from time-dependent perturbation theory. Fermi's golden rule allows us to analyze and understand the dynamics of transitions in quantum systems subjected to external perturbations, such as the interaction with x-ray photons [18].

Hence, taking into account the interaction Hamiltonian as described in equation (2.8), the cross section for the transition from the initial state i to the final state f can be expressed as:

$$\sigma_{if}(\omega) = \frac{4\pi^2\omega\alpha_0^2}{3}\left|\langle\Psi_f|\sum_k r_k|\Psi_i\rangle\right|^2\delta(E_f - E_i - \hbar\omega) \tag{2.10}$$

Where α_0 is the fine structure constant and $\langle\Psi_f|\sum_k r_k|\Psi_i\rangle$ is the dipole matrix elements. The dipole matrix elements play a crucial role in the calculation of the cross section for photoionization. They represent the transition probabilities between initial and final states induced by the interaction of the system with the electromagnetic radiation. Therefore, accurate evaluation of these matrix elements is essential in understanding and predicting the photoionization cross section of a system.

2.1.2 Relativistic effects in the photoionization cross section

Relativistic effects can significantly influence atomic photoionization cross sections. The motion of electrons at high speeds and their interaction with heavy atomic nuclei introduce relativistic corrections that impact the photoionization process. In the presence of high-energy photons or heavy atomic nuclei, relativistic corrections become important. These corrections arise from the relativistic motion of electrons, which can lead to changes in the energy levels and wave functions of the atomic system. One important relativistic effect is the relativistic increase in electron mass, known as mass-energy equivalence. This effect causes the energy levels of the electrons to shift, resulting in changes in the photoionization cross sections. Additionally, relativistic corrections can lead to spin-orbit coupling, where the motion of the electron's spin becomes coupled to its orbital motion, affecting the angular distribution of the photoelectrons. Reference [19] provides a detailed analysis of recent examples that emphasize the notable influence of the spin-orbit interaction on various aspects of atomic photoionization. Furthermore, the relativistic treatment of the electromagnetic interaction between the incident photon and the atomic electrons requires the incorporation of relativistic wave equations, such as the Dirac equation. These equations account for the spin and relativistic effects of the electrons, leading to more accurate calculations of the photoionization cross sections. In Coulomb gauge, the nonrelativistic interaction between the radiation field and the electron momentum can be described by the term exp(ik.r)p, where p represents the electron momentum operator and k is the wave number of the photon. On the other hand, the relativistic interaction is given by exp(ik.r)α, where α denotes the components of the 4x4 Dirac matrices. These expressions emphasize the distinction between the nonrelativistic and relativistic approaches of the interaction between the radiation field and the electron momentum [20]. Relativistic effects play a crucial role in understanding and accurately calculating atomic

photoionization cross sections, especially in situations involving high photon energies or heavy atomic nuclei.

2.2 Relativistic random phase approximation (RRPA):

The Relativistic Random Phase Approximation (RRPA) is a theoretical method used to describe the electronic structure and photoionization processes in relativistic systems. It is an extension of the Random Phase Approximation (RPA) to include relativistic effects. The Relativistic Random Phase Approximation (RRPA) and the Random Phase Approximation (RPA) are both theoretical methods used to study the electronic structure and properties of many-body systems. However, there are some differences between the two approaches, and the RRPA offers advantages over the RPA in certain scenarios. The primary distinction is that the RRPA incorporates relativistic effects, *via* the Dirac equation, which are important in systems where the velocities of the electrons approach the speed of light [60]. In contrast, the standard RPA does not account for relativistic corrections. The RRPA is specifically designed to treat atomic transitions in highly charged ions and atoms, where both electron correlation and relativity are significant. These systems involve strong Coulomb interactions and relativistic velocities, making the inclusion of relativistic effects crucial. The RPA, on the other hand, is more commonly applied to non-relativistic systems. The RRPA involves solving the relativistic Dirac equation for the electrons and includes the effects of electron-electron correlations. It provides a description of the electronic excitations and ionization processes, including the energy levels, transition probabilities, and spectral properties. By incorporating relativistic effects into the RPA framework, the RRPA allows for more accurate calculations of photoionization spectra and cross sections in relativistic systems. It is particularly relevant in studies involving heavy elements or high-energy processes where relativistic effects

cannot be neglected. The RRPA is a method explicitly based on the Dirac equation [21], making it inherently relativistic. It is specifically designed to incorporate relativistic effects in the study of atomic transitions in highly charged ions and atoms. One advantage of the RRPA is that it includes ground state correlations, which account for the interactions between electrons in the initial state. Additionally, it incorporates interchannel couplings of the final state, allowing for configuration interaction in the continuum. This means that the RRPA considers the coupling between different final states during the photoionization process [22]. By including these correlations and couplings, the RRPA improves upon the limitations of Hartree calculations and provides a more accurate description of the electronic structure and dynamics, particularly in systems where both electron correlation and relativistic effects are important. By linearizing the time-dependent Dirac-Fock (DF) equations, the RRPA theory is derived. These equations represent how an atom reacts to a time-dependent external field. The Dirac Hamiltonian for a single electron is described by [23]:

$$h_0 = \vec{\alpha}.\vec{p} + \beta m - {Ze^2}/{m} \tag{2.11}$$

The DF equations for a ground state of an N-electron closed-shell atom is given by:

$$(h_0 + V)u_i = \epsilon_i u_i \qquad i = 1, 2, \dots, N \tag{2.12}$$

where ϵ_i is the orbital eigenvalue and natural units $\hbar = c = 1$, ${e^2}/{\hbar c} = \alpha = 1/137.036$ are employed. The DF potential $V(r)$ is given by:

$$Vu(\vec{r}) = \sum_{j=1}^{N} e^2 \int \frac{d^3r'}{\left|\vec{r} - \vec{r'}\right|}\left[\left(u_j^{\dagger}u_j\right)'u - \left(u_j^{\dagger}u\right)'u_j\right] . \tag{2.13}$$

When a time-dependent external field, represented as $\nu_+ e^{-i\omega t} + \nu_- e^{i\omega t}$, is applied, it induces a time-dependent perturbation in each of the DF orbitals $u_i(\vec{r})$. As a result, the DF orbitals can be expressed as a series expansion that includes the first harmonic as follows:

$$u_i(\vec{r}) \longrightarrow u_i(\vec{r}) + w_{i+}(\vec{r})e^{-i\omega t} + w_{i-}(\vec{r})e^{i\omega t} + \cdots, \tag{2.14}$$

Here $u_i(\vec{r})$ represents the unperturbed DF orbital, and w_{i+}, w_{i-} and so on, correspond to the perturbations induced by the external field at the respective harmonics. The omitted terms in the expansion correspond to higher harmonics. This expansion allows for the incorporation of the time-dependent perturbation induced by the external field into the description of the DF orbitals, enabling the study of the system's response to the applied field at different frequencies. If we consider the Dirac-Coulomb Hamiltonian for N electron atom in a central field of the nucleus of charge Z is [24]:

$$H_{DC} = \sum_{i}^{N} H_D(r_i) + U(r_i) = \sum_{i}^{N} \left(c\alpha_i . p_i + \beta_i c^2 + V_{nuc}(r_i) \right) + \phi(r_i) \, . \tag{2.15}$$

By expanding equation (2.15) in powers of the external field $v_{\pm}$, considering only the first-order terms, yields the following expression:

$$(h_0 + V - \epsilon_i \mp \omega) w_{i\pm} = \left(v_{\pm} - V_{\pm}^{(1)} \right) u_i + \sum_j \lambda_{ij\pm} u_j \qquad i = 1, 2, \dots, N \tag{2.16}$$

The solutions to these inhomogeneous equations (2.16) can be expressed as an expansion using the complete set of solutions to the homogeneous equations. The homogeneous equations are obtained by omitting the "driving" term $v_{\pm}$ from the right-hand side. By considering the solutions to the homogeneous equations, the solutions to the inhomogeneous equations can be constructed and analyzed in terms of this complete set of solutions [23]:

$$(h_0 + V - \epsilon_i) w_{i\pm} + V_{\pm}^{(1)} u_i - \sum_j \lambda_{ij\pm} u_j = \pm \omega w_{i\pm} \qquad i = 1, 2, \dots, N \tag{2.17}$$

In order to maintain the orthogonality of the perturbed orbitals $w_{i\pm}(\vec{r})$ to the occupied orbitals $u_i(\vec{r})$, Lagrange multipliers $\lambda_{ij\pm}$ are introduced in Equation (2.16), and V represents the DF potential, while $V_{\pm}^{(1)}$ corresponds to the first-order perturbation of the expansion of V, and

incorporates electron-electron correlations. The inclusion of $V_{\pm}^{(1)}$allows for the consideration of the effects of electron-electron interactions and correlations on the perturbed orbitals:

$$V_{\pm}^{(1)}u_i = \sum_{j=1}^{N} e^2 \int \frac{d^3r'}{\left|\vec{r}-\overrightarrow{r'}\right|}\left[\left(u_j^{\dagger}w_{j\pm}\right)'u_i + \left(w_{j\mp}^{\dagger}u_j\right)'u_i - \left(w_{j\mp}^{\dagger}u_i\right)'u_j - \left(u_j^{\dagger}u_i\right)'w_{j\pm}\right] \qquad (2.18)$$

Studying the eigenvalue problem is essential as it allows for the expansion of any solution to the inhomogeneous equation (2.16) using eigenfunctions derived from Eq. (2.17). The positive frequency components w_{i+} of the eigenfunctions describe the excited states of the atom (including the continuum), incorporating correlations in the final state, while the negative frequency components w_{i-} capture the effects of correlations in the ground state. These eigenfunctions are subject to an orthogonality constraint [25]:

$$\int d^3r \;\; w_{i\mp}^{\dagger}u_j = 0, \qquad i,j = 1,2,\dots,N \qquad (2.19)$$

The transition amplitude from the ground state to the excited state, characterized by the RRPA functions $w_{i\pm}(\vec{r})$ with frequency ω, can be determined by the perturbations $v_{\pm}$ in terms of vector potential $\vec{A}$:

$$v_+ = e\,\vec{\alpha}.\overrightarrow{A}, \qquad v_- = v_+^{\dagger} \qquad (2.20)$$

This perturbation represents the electron-photon interaction in the Coulomb gauge. The amplitude of this transition is given by:

$$T = \sum_{i=1}^{N} e \int d^3r \,(\, w_{i+}^{\dagger}\,\vec{\alpha}.\overrightarrow{A}u_i + u_i^{\dagger}\vec{\alpha}.\overrightarrow{A}w_{i-}). \qquad (2.21)$$

2.3 Cross section and angular distribution

The differential cross section for photoionization describes the probability of a photon interacting with an atom or molecule and causing ionization with the photoelectron emerging in a particular solid angle range. In terms of the transition amplitude which is described in Eq. (2.21), differential cross section can be expressed using the following formula:

$$\frac{d\sigma}{d\Omega} = \frac{\alpha E p}{2\pi\omega}|T|^2 \tag{2.22}$$

Where E represents the energy of the photoelectron, p represents its momentum, and ω is the energy of the incident photon. Keeping in mind that the multipole transition amplitude in a single-electron approximation is given by:

$$T_{JM}^{(\lambda)} = \int d^3r \; w_i^{\dagger}\vec{\alpha}\,.\,\vec{a}_{JM}^{(\lambda)}u_i = i\left(\frac{2\pi^2}{Ep}\right)^{\frac{1}{2}}\left(\frac{(2J+1)(J+1)}{J}\right)^{\frac{1}{2}}\frac{\omega^J}{(2J+1)!!}\sum_{\bar{\kappa}\bar{m}}(\chi_v^{\dagger}\,\Omega_{\bar{\kappa}\bar{m}}(\hat{p}))$$

$$(-1)^{\bar{j}-\bar{m}}\begin{pmatrix}\bar{j} & J & j\\ -\bar{m} & M & m\end{pmatrix} i^{1-\bar{l}}e^{i\delta_{\bar{k}}}\left\langle\bar{a}\middle\|Q_J^{(\lambda)}\middle\|a\right\rangle(-1)^{\bar{j}+j+J} \tag{2.23}$$

Where E and $\hat{p}$ are the photoelectron energy and momentum direction. ω is the photon frequency, and $\delta_{\bar{k}}$ is the phase of the continuum wave with $\bar{k} = \mp(\bar{j}+1/2)$ for $\bar{j} = (\bar{l} \pm \frac{1}{2})$. The spherical spinor which is a function of Clebsch-Gordan coefficients and spherical harmonics Y_{lm}, and two component spinors χ_v. The spherical spinor is defined as:

$$\Omega_{km}(\hat{n}) = \sum_{v=\pm1/2} C^{jM}_{l,M-v,1/2v}\, Y_{lm-v}(\hat{n})\; \chi_v \tag{2.24}$$

and $v = \pm\frac{1}{2}$ is the photoelectron spin polarization.

The reduced matrix element of an electric or magnetic multipole operator between initial state a and final state $\bar{a}$ is equal to:

$$\left\langle\bar{a}\middle\|Q_J^{(\lambda)}\middle\|a\right\rangle = (-1)^{j+1/2}[\,\bar{j}\,]\,[\,j\,]\begin{pmatrix}j & \bar{j} & J\\ -1/2 & 1/2 & 0\end{pmatrix}\times\pi(\bar{l},l,J-\lambda+1)R_J^{(\lambda)}(\bar{a},a) \tag{2.25}$$

$R_J^{(\lambda)}(\overline{a}, a)$ is the radial integral and π is the parity factor. By summing over spins of the continuum electron and summing over the entire closed subshell $n\kappa$, we consider the total contribution from all possible spin states of the outgoing electron and sum over all the electrons within the closed subshell $n\kappa$:

$$\frac{d\sigma_{n\kappa}}{d\Omega} = \frac{\alpha\pi}{2\omega}\sum_{L=0}^{\infty} A_L\, P_L(\cos\theta) \tag{2.26}$$

where θ is the angle between the electron and photon momentum vectors and A_L is given by [23, 25]:

$$A_L = \sum_{J,J',\lambda,\lambda',\overline{\kappa},\overline{\kappa'}} B\left(J, J', \overline{\kappa}, \overline{\kappa'}, L, j\right)\left(\frac{(J+1)(J'+1)}{JJ'}\right)^{\frac{1}{2}}\left(\frac{\omega^{J+J'}}{(2J-1)!!\,(2J'-1)!!}\right)$$
$$\times\left(i^{J-\lambda-\bar{l}+1}e^{i\delta_{\overline{k}}}\left\langle\overline{a}\middle\|Q_J^{(\lambda)}\middle\|a\right\rangle\right)\left(i^{J'-\lambda'-\bar{l}'+1}e^{i\delta_{\kappa'}}\left\langle\overline{a'}\middle\|Q_{J'}^{(\lambda')}\middle\|a\right\rangle\right). \tag{2.27}$$

A_L is a function of ω which depends on the reduced matrix elements $\left\langle\overline{a}\middle\|Q_J^{(\lambda)}\middle\|a\right\rangle$ of the multipole moment operator $Q_J^{(\lambda)}$ and λ=1 (0) represents electric (magnetic) multipole. J and J' are the total angular momenta of the electron of initial and final states. When integrating equation (2.26) over the directions in which the outgoing electrons propagate, the obtained result is an expression that accounts for the contributions from all possible photoelectron emission angles. This integration allows for a comprehensive analysis of the system's behavior in terms of the specific quantities and parameters. Upon performing the integration over the outgoing electron directions of equation (2.26), the resulting expression is obtained:

$$\sigma_{nk}(\omega) = \frac{2\pi^2\alpha}{\omega}A_0 = \frac{2\pi^2\alpha}{\omega}\sum_{J\lambda\overline{k}}\frac{(J+1)}{J(2J+1)}\,\frac{\omega^{2J}}{[(2J-1)!!]^2}\left\langle\overline{a}\middle\|Q_J^{(\lambda)}\middle\|a\right\rangle \tag{2.28}$$

In our formulation, Eqs. (2.27) and (2.28) were initially expressed in terms of the single-electron reduced matrix element. However, we have the flexibility to substitute the single-particle reduced matrix elements with the corresponding many-particle expressions given by:

$$\left\langle \overline{a}\left\| Q_J^{(\lambda)} \right\| a \right\rangle_{RRPA} = \sum_{\overline{b}} \left(\left\langle \overline{b_+}\left\| Q_J^{(\lambda)} \right\| b \right\rangle \right) + \left(\left\langle \overline{b_-}\left\| Q_J^{(\lambda)} \right\| b \right\rangle \right), \quad (2.29)$$

$\left\langle \overline{b_\pm}\left\| Q_J^{(\lambda)} \right\| b \right\rangle$ being the reduced matrix elements in the many-particle expressions. By employing these many-particle expressions, we can obtain the results within the framework of the RRPA. This substitution allows us to consider the collective behavior of the system and incorporate the interactions between multiple particles, providing a more comprehensive description of the physical phenomena under investigation.

2.3.1 Electric dipole transitions

In the electric dipole approximation, the differential cross section for photoionization of an unpolarized target by incident linearly polarized light can be expressed as follows [27]:

$$\left[\frac{d\sigma_{nk}}{d\Omega}\right]_{lin\ pol} = \frac{\sigma_{nk}(\omega)}{4\pi}\left[1 + \beta_{nk}(\omega) p_2(\cos\theta)\right] \quad (2.30)$$

In this context $\sigma_{nk}(\omega)$ represents the total photoionization cross section, β denotes the asymmetry parameter, and (θ) is the angle of the photoelectron momentum with respect to the polarization vector of the incident light, $p_2(\cos\theta) \equiv \frac{1}{2}(3cos^2(\theta) - 1)$ and $n\kappa$ is initial state for photoionization of a closed-shell atom. An electric dipole interaction has the potential to excite electrons in the subshell $n\kappa$ to states with $\overline{\kappa} = -\kappa, \kappa \pm 1$. This phenomenon arises from the interaction between the electric dipole and the electrons, which results in transitions between angular momentum states within the nκ subshell. κ is defined as $\kappa = \mp\left(j + \frac{1}{2}\right)$ where $j = l \pm 1/2$. The parameters n and κ represent the principal and angular quantum numbers, respectively. These quantum numbers describe the energy level and the specific orbital characteristics of an electron within an atom. Additionally, the parameters j and l correspond to the total and orbital angular momentum quantum numbers. To calculate the electric dipole cross-section, a shorthand notation

represented for the reduced matrix element as $D_{j\to\bar{j}} = i^{1-\bar{l}} e^{i\delta_{\overline{\kappa}}} \left\langle \overline{\kappa} \middle|\middle| Q_J^{(\lambda)} \middle|\middle| \kappa \right\rangle_{RRPA}$. This notation allows us to denote the interaction between the initial and final states through the multipole moment operator, denoted by $Q_J^{(\lambda)}$, [23, 25]:

$$\sigma_{nk} = \frac{4\pi^2\alpha}{3}\omega\left(\left|D_{j\to j-1}\right|^2 + \left|D_{j\to j}\right|^2 + \left|D_{j\to j+1}\right|^2\right) \tag{2.31}$$

where α is the fine structure constant and ω is the photon energy. Electric dipole asymmetry parameter is given by [26]:

$$\beta_{nk}(\omega) = \left\{\frac{1}{2}\frac{(2j-3)}{2j}\left|D_{j\to j-1}\right|^2 - \frac{3}{2j}\left(\frac{2j-1}{2(2j+2)}\right)^{\frac{1}{2}}\left(D_{j\to j-1}D^*{}_{j\to j} + c.c.\right) - \frac{(2j-1)(2j+3)}{(2j)(2j+2)}\left|D_{j\to j}\right|^2 - \right.$$

$$\frac{3}{2}\left(\frac{(2j-1)(2j+3)}{2j(2j+2)}\right)^{\frac{1}{2}}\left(D_{j\to j-1}D^*{}_{j\to j+1} + c.c.\right) + \frac{1}{2}\frac{(2j+5)}{(2j+2)}\left|D_{j\to j+1}\right|^2 + \frac{3}{(2j+2)}\left(\frac{2j+3}{2(2j)}\right)^{\frac{1}{2}}\left(D_{j\to j}D^*{}_{j\to j+1} + \right.$$

$$\left.\left. c.c.\right)\right\}\left(\left|D_{j\to j-1}\right|^2 + \left|D_{j\to j}\right|^2 + \left|D_{j\to j+1}\right|^2\right)^{-1} \tag{2.32}$$

Equation (2.30) clearly shows that the angular distribution is entirely dependent on the asymmetry parameter β. This parameter contains all the necessary dynamical information regarding the angular distribution. It is important to note that the magnitude of the asymmetry parameter β is constrained within the range of -1 ≤ β ≤ 2 due to the requirement that $\frac{d\sigma_{nk}}{d\Omega}$ remains positive for all values of θ [27].

2.4 Application of RRPA to the photoionization of superheavy elements:

We calculated photoionization cross sections of the ground states of superheavy atoms No (Z = 102), Cn (Z = 112), and Og (Z = 118) using fully relativistic methodologies as presented in Ref. [28]. The atomic aspects of these super heavy elements have not been extensively studied experimentally due to the short-lived nature of their nuclei. As a result, theoretical calculations

and predictions are required to understand the properties of these elements. The photoionization of the ground states of these superheavy atoms is investigated using the relativistic random-phase approximation (RRPA) methodology [23, 25] which takes into account both relativistic and many-body electron-electron correlation effects. These effects can have a significant impact on the photoionization cross sections of atoms, and understanding their interplay is crucial for accurately predicting the behavior of these elements. The RRPA method uses Dirac-Fock (DF) energies in its calculations. The DF threshold energies represent the energy levels at which electron excitations occur within the relativistic framework of the Dirac-Fock theory. The DF threshold energies for different subshells, which correspond to specific electron orbitals within an atom are calculated and presented in table (2.4.1). The subshell ordering refers to the arrangement of these electron orbitals based on their energy levels. The DF threshold energies and subshell ordering provided in Table (2.4.1) serve as a foundation for the RRPA calculations. The RRPA method utilizes this information to investigate and predict various atomic properties, such as excitation energies, transition probabilities, and spectral characteristics, incorporating the relativistic effects that play a significant role in atomic systems. As an example, we discuss the application of the RRPA method to study the heaviest element, Oganesson (Og) [28]. Oganesson, represented by the symbol Og, is a synthetic chemical element with an atomic number of 118. It was first created in 2002 and has an atomic mass of 294. Of all known elements, Oganesson has the highest atomic number and atomic mass. It is radioactive and highly unstable. On the periodic table, Oganesson is located in the noble gas column, below radon. Electron configuration for $^{118}\mathbf{Og}$ is $[Rn]5f^{14}\ 6d^{10}\ 7s^2\ 7p^6$. In our study, we have performed calculations to determine the binding energies associated with each subshell of the ground states of the Og element. These calculations were conducted using the DF equations, which were previously explained and introduced in detail. The obtained binding

energies for each subshell (table 2.1) serve as essential inputs for subsequent calculations involving photoionization processes.

Table 2-1 Binding energies of the subshells (in atomic units, 27.211 eV) of the ground states of the element Og (Z = 118).

Subshell	Binding energy (a.u.)
1s	8185.135
2s	1718.755
$2p_{1/2}$	1681.706
$2p_{3/2}$	1138.546
3s	471.181
$3p_{1/2}$	451.724
$3p_{3/2}$	318.335
$3d_{3/2}$	286.65
$3d_{5/2}$	265.676
4s	140.972
$4p_{1/2}$	131.02

Subshell	Binding energy (a.u.)
$4p_{3/2}$	92.024
$4d_{3/2}$	76.265
$4d_{5/2}$	70.35
$4f_{5/2}$	49.792
$4f_{7/2}$	48.043
5s	39.884
$5p_{1/2}$	35.183
$5p_{3/2}$	23.663
$5d_{3/2}$	16.663
$5d_{5/2}$	15.07
6s	8.987

Subshell	Binding energy (a.u.)
$6p_{1/2}$	7.077
$5f_{5/2}$	6.511
$5f_{7/2}$	6.141
$6p_{3/2}$	4.216
$6d_{3/2}$	1.764
$6d_{5/2}$	1.493
7s	1.297
$7p_{1/2}$	0.739
$7p_{3/2}$	0.306

Regarding the valence structure and ordering of this element, it follows a normal pattern except for a noteworthy observation that is presented in the table (2.1). the 5f subshells are found to be positioned between the $6p_{1/2}$ and $6p_{3/2}$ subshells. This deviation from the expected ordering is quite interesting. Furthermore, an important characteristic of this arrangement is the substantial splitting between the $6p_{1/2}$ and $6p_{3/2}$ subshells, which is due to spin-orbit splitting.

2.4.1 Results and discussion:

In this research [28], all relativistic single-excitation channels arising from the outermost subshell down to the 4f channels are considered in the calculations. To perform these calculations, the existing RRPA code was modified and upgraded to deal with larger numbers of subshells and channels. The fully relativistic methodology is used to explore the response of superheavy atoms to electromagnetic radiation. The total photoionization cross section for Og (atomic number 118) was calculated. The cross section was computed from the energy threshold up to a photon energy of 60 atomic units (a.u.), equivalent to 1632.72 electron volts (eV).

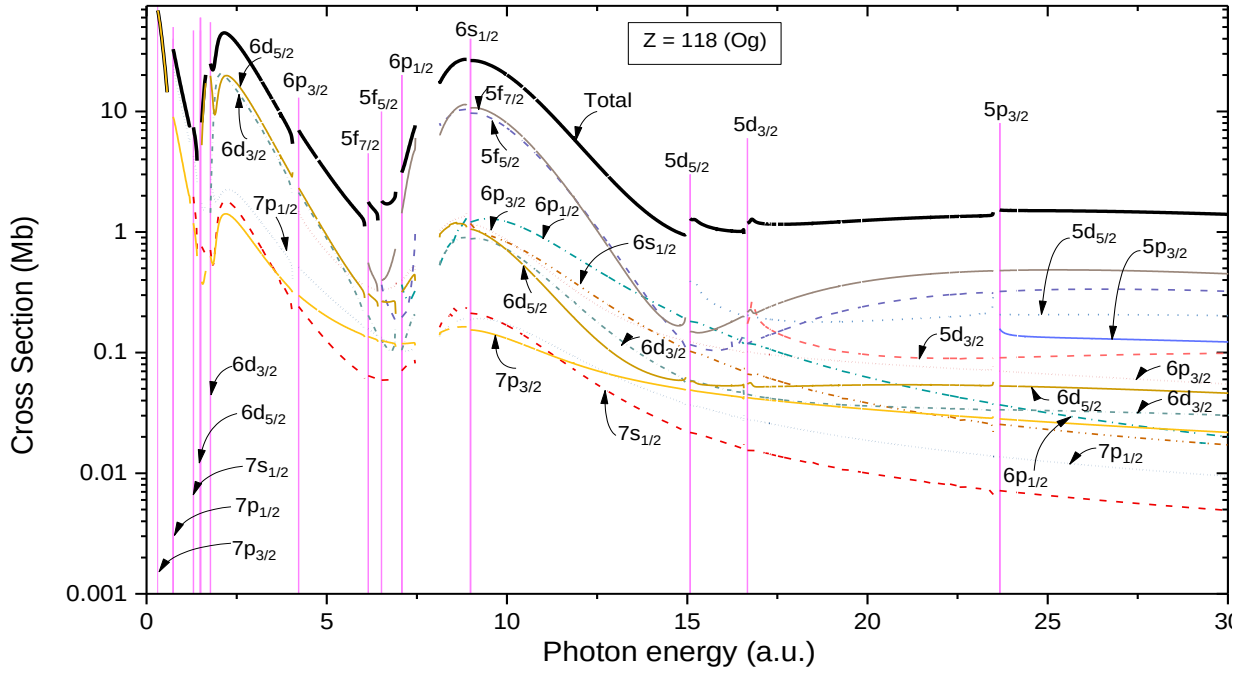

Figure 2-1 Photoionization cross section for Og from threshold to 30 a.u. The vertical lines in the curve indicate the various subshell thresholds.

The results are presented in two plots: Figure 2.1 showing the cross section from zero to 30 a.u., and Figure 2.2 displaying the cross section from 30 to 60 a.u.

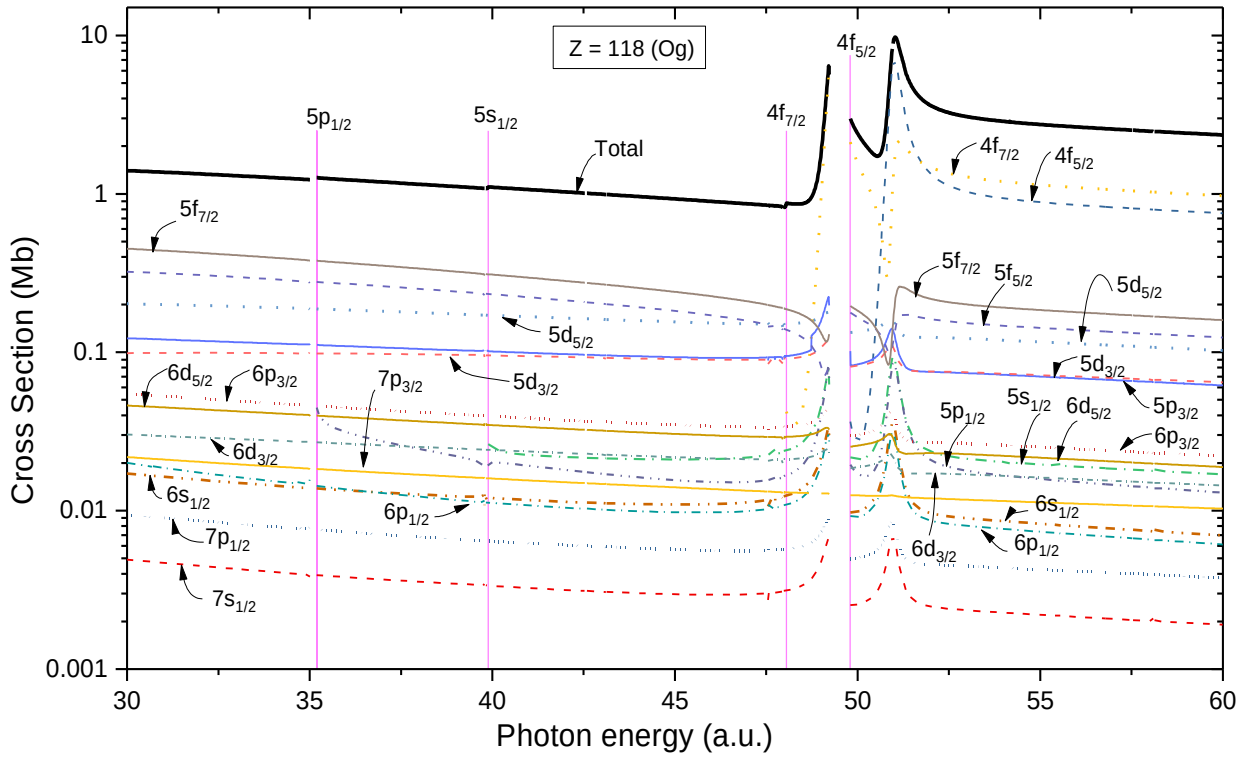

Figure 2-2 Photoionization cross section for Og from 30 a.u. to 60 a.u. The vertical lines in the curve indicate the various subshell thresholds. The autoionizing states below each inner threshold are omitted for simplicity.

These plots provide a visual representation of how the photoionization cross section of Og varies with increasing photon energy, allowing for a better understanding of the ionization behavior in this element. This element consists of 31 relativistic subshells of which we've considered 17 subshells from $7p_{3/2}$ to $4f_{5/2}$ resulting in 45 coupled relativistic channels. It is worth noting that the channels that were excluded from the analysis were located at higher energy levels, and their omission did not significantly impact the results. There is a gap of a few eV below each inner threshold. These regions are known as autoionizing resonance regions and were intentionally excluded from the analysis. These regions were excluded from the calculation to focus specifically on the primary features of interest. Over the majority of the energy range considered, the 6d, 5f, and 4f subshells were found to dominate the total cross section. However, in the region of the 5f

Cooper minima [51], the 5d subshells demonstrated dominance over a small energy range. Cooper minima occur due to a change in sign of the partial-wave photoionization matrix element within a specific ionization channel. This change is a result of the energy-dependent radial overlap between the continuum and bound wave functions. Notably, Cooper minima are observed only when the radial wave function of the initial state contains at least one node [54] [see appendix A]. These findings emphasized the importance of interchannel coupling in the photoionization process of Og. In regions where the 6d subshells dominated, the cross sections of the weaker subshells mirrored the behavior of the 6d subshells. Similar trends were observed in the region of the 5f shape resonances. To see this quantitatively, consider the equation (2.33) for fully coupled dipole matrix element $D_i(E)$ in terms of uncoupled matrix element $M_j(E)$:

$$D_i(E) = M_i(E) + \sum_j \int dE' \frac{\langle \psi_i(E) | H - H_0 | \psi_j(E') \rangle}{E - E'} M_j(E') \qquad (2.33)$$

where $\psi_i(E)$ and $\psi_j(E')$ are final continuum state wave functions of channels i and j and with energies E and E' respectively. $H - H_0$ represents the perturbation Hamiltonian. It is evident that the subshell cross sections are primarily influenced by the second term, the perturbation term, in the equation. In the case where the channel i represents the 7s state and the channels j represent the 4f states, equation (2.33) illustrates that when the 4f dipole matrix elements significantly surpass the 7s matrix element, the first term on the right-hand side of the equation (representing the 7s matrix element) is significantly smaller compared to the second term (representing the first-order perturbation). Consequently, based on this equation, the 7s matrix element and the corresponding cross section will be strongly influenced by interchannel coupling with the cross sections of the 4f states.

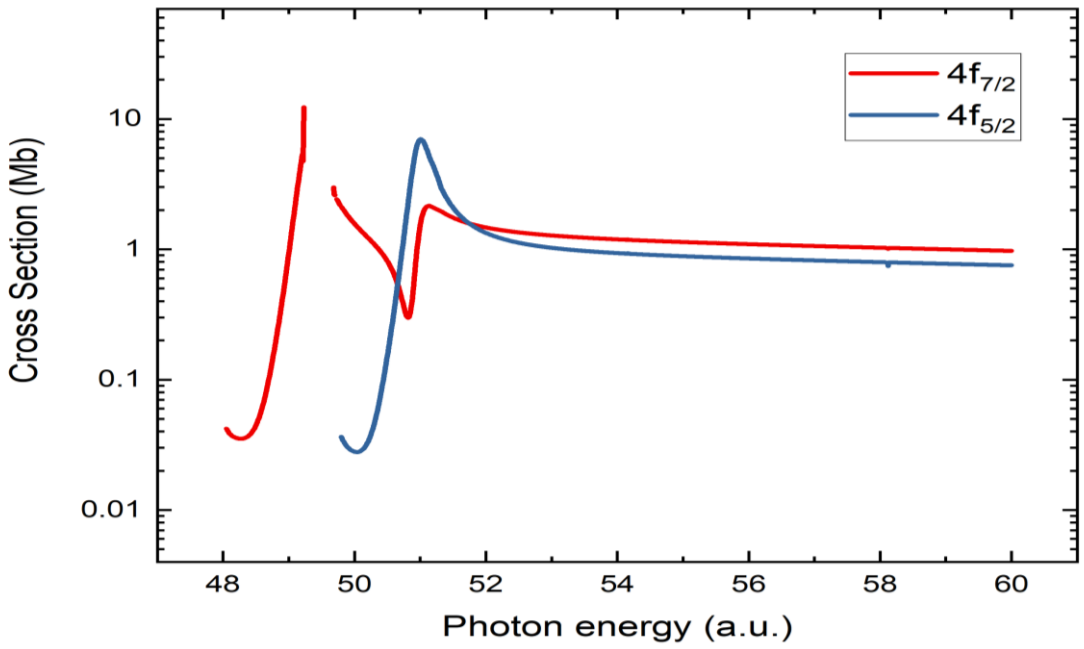

Figure 2-3 Photoionization of the 4f subshells of Og (Z = 118). The autoionizing states below the $4f_{7/2}$ threshold are omitted for simplicity.

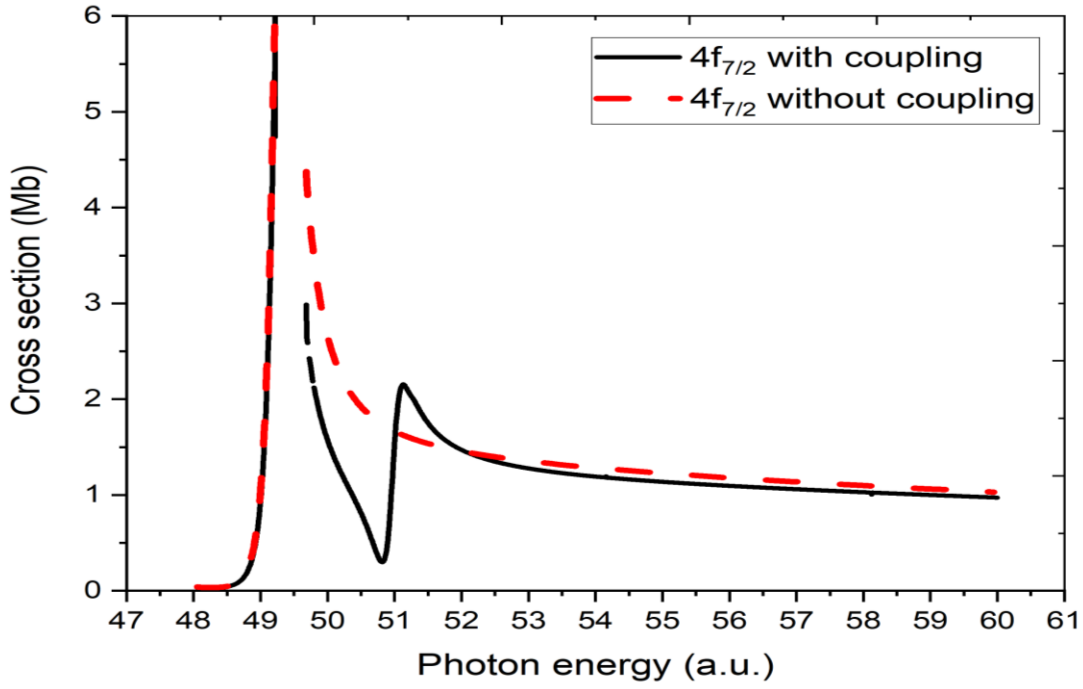

Figure 2-4 Photoionization of the 4f subshells of Og (Z = 118) with and without coupling.

The photoionization channels associated with the 4f subshells in Og demonstrate a remarkable and pronounced spin–orbit-interaction-activated interchannel coupling (SOIAIC) effect [see appendix B], which is shown in Figure 2.3. Specifically, the cross section of the $4f_{7/2}$ subshell, when considered without interchannel coupling (as shown in Figure 2.4), exhibits a steady decrease from the peak of the shape resonance. However, when interchannel coupling is introduced, a significant reduction, or deep minimum, in the cross section occurs near the shape resonance of the $4f_{5/2}$ subshell. Due to the spin-orbit interaction, the 4f subshells undergo a splitting into a doublet, resulting in an interchannel interaction between the photoionizing channels associated with each member of the doublet, specifically between the $4f_{7/2}$ and $4f_{5/2}$ channels. The existence of such relativistic interactions is not unique to Og and can be expected in other high-Z atoms. With the exception that the studied atomic system consists of closed subshell configurations, there is no particular distinction for Og compared to neighboring atoms in the periodic table. Consequently, it becomes evident that similar interchannel coupling effects in photoionization can be anticipated in all super heavy elements. In summary, the phenomenology described possesses a general applicability to a broad range of systems [28].

3 TIME DELAY

Time delay in atomic photoionization refers to the brief delay that occurs between the absorption of a photon and the release of the photoelectron wave packet. This delay is incredibly small, typically measured in attoseconds (1 as = $10^{-18}\ s$) . Despite its small size, this delay carries important information about the photoionization process and can provide insights into the underlying dynamics of the system. The concept of time delay in atomic photoionization can be traced back to pioneering works by Wigner [29], Eisenbud [55], and Smith [56], who introduced the idea of temporal delays in quantum scattering processes. These early theoretical developments laid the groundwork for understanding the time-dependent aspects of quantum dynamics during photoemission. Subsequently, studies by Kheifets and Ivanov [30] provided theoretical insights into the role of multiple scattering channels and their influence on time delay measurements. They highlighted the significance of phase shifts and quantum interference effects in shaping the temporal behavior of photoelectrons. The study of time delay has required the use of advanced experimental techniques that can capture electron movement. The introduction of attosecond science and ultrafast laser pulse technology has been a game-changer in this field. The groundbreaking work of Eckle et al. [31] was a significant milestone in time delay studies. Using advanced attosecond streak cameras, they successfully measured time delay in the photoionization of neon. This innovative experiment allowed them to directly observe and accurately quantify time delay effects, providing new insights into the ultrafast behavior of electrons during atomic photoionization. This achievement demonstrated the feasibility of measuring time delay and opened up exciting possibilities for further exploration of attosecond phenomena. Building upon these achievements, Pazourek et al. [32] introduced the angular streaking technique, providing a robust method to extract photoemission time delays with high precision. This angular-resolved

approach opened new avenues for investigating the temporal behavior of photoelectrons in various atomic and molecular systems. The implications of time delay measurements extend beyond atomic and molecular physics, encompassing a wide range of scientific disciplines. The ability to probe ultrafast dynamics at the attosecond time scale has led to numerous applications and potential breakthroughs. In materials science, studies by Schultze et al. [33] demonstrated how time delay measurements can provide crucial insights into the electronic structure and photoemission processes in solid-state systems. Such understanding is valuable for designing and optimizing advanced materials for future technologies. Moreover, the field of attosecond spectroscopy has been significantly enriched by time delay investigations. Haessler et al. [34] showcased the relevance of time delays in probing ultrafast electron-electron interactions, leading to a deeper comprehension of electron correlation effects. In recent experimental and theoretical studies, researchers have identified the importance of considering relativistic effects to accurately interpret photoionization time delay measurements. The utilization of innovative techniques offers a unique opportunity for precise calibration of measuring devices and the study of electron motion in atoms, molecules, and solids on the incredibly short attosecond time scale.

These cutting-edge devices, namely the attosecond streak camera, angular streaking attoclock, and RABITT, make use of a phase-stabilized electric field generated by short laser pulses. This electric field enables the conversion of the release time of emitted electrons into measurable quantities, such as kinetic energy, momentum vector, and electron detector signals [35]. The attosecond streak camera [36] is designed to capture the ultrafast dynamics of electron wave packets, allowing researchers to investigate the temporal behavior of electronic processes with exceptional precision. On the other hand, the angular streaking attoclock [37] focuses on determining the electron's momentum vector, offering valuable insights into the directionality of

electron ejection. The RABITT technique [38], based on the reconstruction of attosecond bursts by ionization of two-photon transitions, enables the study of electronic dynamics with great sensitivity. By detecting the beating signal of the emitted electrons, RABITT provides valuable temporal information, further advancing our understanding of quantum dynamics. Through the implementation of these methodologies, scientists gain a deeper understanding of the underlying physics governing attosecond-scale processes, offering critical insights into fundamental atomic and molecular interactions. Moreover, the knowledge gained from attosecond science bears substantial implications for various fields, including materials science, ultrafast spectroscopy, quantum computing, and laser technology. The unprecedented capabilities of the attosecond streak camera, angular streaking attoclock, and RABITT devices open up new horizons for the study of ultrafast electron motion. These techniques not only enhance our understanding of quantum phenomena but also hold the potential to drive significant advancements in diverse scientific and technological applications, paving the way for exciting discoveries in the near future.

A distinct concept of delay-time associated with collisions has been discovered by Bohm, Eisenbud, and Wigner through a wave-packet analysis. Specifically, when considering elastic scattering, which can be described using a simple phase shift (η), they demonstrate that an appropriate definition of delay-time involves the energy derivative of this phase shift. In other words, the delay time refers to the time delay experienced by a wave packet during the scattering event, particularly in the context of elastic collisions. The phase shift (η) represents the phase change experienced by the wave function of the scattering particles due to the interaction with a potential. Bohm [39], Eisenbud [40], and Wigner [41] propose that the delay time can be quantified by calculating the energy derivative of the phase shift (η) with respect to the energy of the particles involved in the collision process:

$$\Delta t = \hbar \frac{d\eta}{dE}. \quad (3.1)$$

This energy derivative based definition provides insights into how the phase shift varies with energy and, in turn, describes the temporal behavior of the scattering wave packet.

3.1 Wigner time delay

In the realm of cutting-edge XUV/IR two-photon ionization experiments, researchers have been investigating the atomic time delay (τ_a) phenomenon, which intriguingly consists of two distinct and crucial components, denoted as τ_W and τ_{CLC} [42]:

$$\tau_a = \tau_W + \tau_{CLC} \quad (3.2)$$

The first component, known as the Wigner time delay (τ_W), is intricately associated with the absorption of XUV (Extreme Ultraviolet) photons during the ionization process. This time delay parameter has been of great interest as it can be linked to the concept of the photoelectron group delay, a key factor in understanding the temporal behavior of the photoelectron wave packet [41]. The second component, referred to as the Coulomb-Laser Coupling (CLC) time delay (τ_{CLC}), emerges from the absorption of IR (Infrared) photons. This intriguing aspect of the time delay arises due to the coupling between the intense IR laser field and the Coulomb field of the ionized particle. It is also commonly known in the scientific literature as the continuum-continuum CC correction. While both τ_W and τ_{CLC} significantly contribute to the overall atomic time delay (τ_a) and play vital roles in shaping the dynamics of the ionization process, researchers often tend to emphasize on the Wigner time delay (τ_W). The importance of τ_W lies in its direct connection to XUV photon absorption, which plays a crucial role in understanding the photoelectron group delay phenomenon. In contrast, the Coulomb-laser coupling component is regarded with somewhat lesser attention during the analysis. The rationale behind this lies in the observation that the CLC

correction rapidly diminishes with increasing energy of the photoelectron. Nevertheless, this intriguing aspect of the atomic time delay still warrants exploration and consideration to gain a comprehensive understanding of the ionization dynamics in XUV/IR two-photon experiments. While the scientific community predominantly focuses on the Wigner time delay, the significance of the Coulomb-laser coupling component cannot be disregarded, providing a captivating avenue for further exploration and understanding in this field of research.

3.2 Photoionization amplitude

We use the multichannel RRPA [23, 25] to calculate the transition amplitude from the ground state u_i to an excited state $\omega_{i\pm}$ when we apply an external field $v_+e^{-i\omega t} + v_-e^{i\omega t}$:

$$T = \sum_{i=1}^{N} \int d^3r \left(\omega_{i+}^{\dagger}\ \vec{\alpha}.\overrightarrow{A}u_i + \ u_i^{\dagger}\ \vec{\alpha}.\overrightarrow{A}\omega_{i-}\right) \tag{3.3}$$

where $\overrightarrow{A}$ is the vector potential and $\vec{\alpha} = \begin{pmatrix} 0 & \vec{\sigma} \\ \vec{\sigma} & 0 \end{pmatrix}$ is the Dirac matrix consisting of Pauli spin matrices. In the single active electron approximation, a detailed multipole transition amplitude is simplified and reduced to a form that involves considering only a single active electron's contribution:

$$T_{JM}^{(\lambda)} = \int d^3r\ \ \omega_{i+}^{\dagger}\ \vec{\alpha}.\vec{a}_{JM}^{\lambda}\ \ u_i \tag{3.4}$$

This approximation is particularly useful in cases where the electron-electron interaction effects are less pronounced, allowing for a more tractable analysis of the multipole transitions within the system. In this equation, the indices J and M represent the photon's angular momentum and its projection, respectively. The parameter λ takes on values of 1 or 0, corresponding to electric or magnetic multipoles, respectively. M = 0 corresponds to linear polarization in the z-direction. Specifically, in the context of a one-electron transition, the equation pertains to the transition from

an initial state characterized by the quantum numbers ljm to a final continuum state denoted by $\bar{l}\,\bar{j}\,\overline{m}$, respectively. The spin of electron in this transition is described by a two-component spinor χ_v. This mathematical expression captures the interaction dynamics and quantifies the probabilities associated with the specific one-electron transition process, aiding in the study of atomic and molecular systems and their responses to electromagnetic fields. This equation becomes [23,25,42]:

$$T_{JM}^{(\lambda)} = i\sqrt{\frac{2\pi^2}{EP}}\sqrt{\frac{(2J+1)(J+1)}{J}}\frac{\omega^J}{(2J+1)!!} \times \sum_{\bar{k}\bar{m}}[\chi_v^{\dagger}\,\Omega_{\bar{k}\bar{m}}(\hat{p})]\,(-1)^{\bar{j}-\bar{m}}\begin{pmatrix}\bar{j} & J & j\\ -\overline{m} & M & m\end{pmatrix}\times$$

$$i^{1-\bar{l}}e^{i\delta_{\bar{k}}}\left\langle \bar{a}\middle|Q_J^{(\lambda)}\middle|a\right\rangle(-1)^{\bar{j}+j+J} \tag{3.5}$$

where E and $\hat{p}$ are the photoelectron energy and momentum direction, ω is the photon frequency, and the spherical spinor which is a function of Clebsch-Gordan coefficients and spherical harmonics Y_{lm}, and two component spinors χ_v. The spherical spinor is defined as:

$$\Omega_{km}(\hat{n}) = \sum_{v=\pm 1/2} C_{l,M-v,1/2v}^{jM}\, Y_{lm-v}(\hat{n})\;\chi_v \tag{3.6}$$

and $v = \pm\frac{1}{2}$ is the photoelectron spin polarization. By considering a shorthand for reduced matrix element:

$$D_{lj\to\bar{l}\,\bar{j}} = i^{1-\bar{l}}e^{i\delta_{\bar{k}}}\left\langle \bar{a}\middle|Q_J^{(\lambda)}\middle|a\right\rangle \tag{3.7}$$

As previously mentioned, $D_{lj\to\bar{l}\,\bar{j}}$ represents the reduced matrix element, a crucial quantity in our calculations. The values of these reduced matrix elements are obtained from the codes that we use for our analyses. These codes allow us to compute and extract the necessary information to determine the reduced matrix elements, which play a key role in understanding the relevant physical processes under investigation, the transition amplitude reduces to:

$$T_{JM}^{(\lambda)} = \sum_{\bar{k}\bar{m}} C_{l,M-v,1/2v}^{jM}\, Y_{lm-v}(\hat{n})\,\chi_v\,(-1)^{\bar{j}-\bar{m}}\begin{pmatrix}\bar{j} & J & j\\ -\overline{m} & M & m\end{pmatrix}\times D_{lj\to\bar{l}\,\bar{j}}\,(-1)^{\bar{j}+j+J} \tag{3.8}$$

Each amplitude is associated with its own photoelectron group delay, which is defined as the Wigner time delay [41]. The Wigner time delay is a measure of the amount of delay or advance experienced by colliding particles during their interaction with the scattering potential. In the context of photoionization, it characterizes the timing of the process of electron emission from an atom after the absorption of a photon. Wigner time delay is defined as [42]:

$$\tau = \frac{\partial \eta}{\partial E}, \qquad \eta = tan^{-1}\frac{[Im\, T_{JM}^{\lambda\nu}]}{[Re\, T_{JM}^{\lambda\nu}]} \tag{3.9}$$

3.3 Electric dipole transitions:

An electric dipole transition occurs when an electron in an atom interacts with the electromagnetic field, causing it to change energy levels. In the domain of electric dipole transitions, we focus on cases where λ=1 and J=1, and we set M=0, signifying a specific linear polarization of the photon. Here, λ=1 implies an electric nature, while J=1 corresponds to dipole transitions. Moreover, M=0 denotes linear polarization along the z direction. Our methodology involves a general formula:

$$[T_{10}^{1\pm}]_{\nu=\pm 1/2} = \sum_{\bar{k}\bar{m}} C_{l,M-\nu,1/2\nu}^{jM}\, Y_{lm-\nu}(\hat{n})\, \chi_\nu\, (-1)^{\bar{j}-\bar{m}} \begin{pmatrix} \bar{j} & 1 & j \\ -\bar{m} & 0 & m \end{pmatrix} \times D_{lj\to\bar{l}\,\bar{j}}\, (-1)^{\bar{j}+j+1} \tag{3.10}$$

to compute transition amplitudes, the crucial factor in electric dipole transitions. However, these transitions adhere to specific guidelines known as selection rules. To be permissible, transitions need to fulfill particular criteria, including Δj=0, ±1 and ΔM_j =0, ±1. Let's consider a transition from the np state. Photoabsorption from an initial $np_{1/2}$ state leads to final states $\epsilon s_{1/2}$ and $\epsilon d_{3/2}$. Hence, by determining the transition amplitude, which has already been derived, we gain the capability to calculate both the phase and the corresponding time delay. An electric dipole transition from a $np_{1/2}$ initial state leads to the following ionization channels:

$np_{1/2} \rightarrow \epsilon s_{1/2}, \epsilon d_{3/2}$, using equation (3.10), we derived the following expressions for the $np_{1/2}$ ionization amplitude:

$$[T_{10}^{1+}]_{np_{1/2}}^{m=1/2} = +\frac{1}{\sqrt{15}} Y_{20}\, D_{np_{1/2}\rightarrow\epsilon d_{3/2}} + \frac{1}{\sqrt{5}} Y_{00}\, D_{np_{1/2}\rightarrow\epsilon s_{1/2}} \quad (3.11)$$

$$[T_{10}^{1-}]_{np_{1/2}}^{m=1/2} = -\frac{1}{\sqrt{10}} Y_{21}\, D_{np_{1/2}\rightarrow\epsilon d_{3/2}} \quad (3.12)$$

Each amplitude is linked to its specific photoelectron group delay, recognized as the Wigner time delay [42], and is defined as follows:

$$\eta = \tan^{-1}\frac{[Im\, T_{10}^{1\pm}]}{[Re\, T_{10}^{1\pm}]}, \qquad t = \frac{d\eta}{dE} \quad (3.13)$$

where η is the phase shift and t represents the Wigner time delay.

3.4 Electric quadrupole transitions:

Within the domain of photoionization time delay calculations, the exploration of electric quadrupole transitions offers a distinctive perspective. Electric quadrupole transitions represent a distinct category of quantum transitions that go beyond the conventional electric dipole transitions. An electric quadrupole is characterized by a distribution of charges that resembles a specific configuration of two electric dipoles. This arrangement interacts with the existing electric fields at the nuclear positions. Just as in the case of electric dipole transitions, selection rules play an important role in electric quadrupole transitions as well. These rules delineate which transitions are possible to occur based on the conservation of angular momentum and other quantum properties. In the case of electric quadrupole transitions, the allowed transitions follow selection rules involving changes in the quantum number of angular momentum (Δj) and the quantum number associated with the projection of angular momentum (ΔM_j). The selection rules for electric quadrupole transitions in a hydrogen-like atom are: $\Delta j = 0, \pm 1, \pm 2, \Delta M_j = 0, \pm 1, \pm 2,$ while

$j = 0 \nrightarrow 0,1;\ 1/2 \nrightarrow 1/2$. The combination of electric quadrupole a dipole transitions into photoionization time delay calculations adds an additional layer of complexity to the analysis, yielding a comprehensive view of the temporal aspects of quantum interactions. The process is repeated for quadrupole transitions, albeit with distinct selection rules in play. For quadrupole transitions $\lambda = 1, J = 2, M = 0$ where λ=1 means electric and, J=2 represents quadrupole transitions and we consider M=0 which means linear polarization in z direction. For electric quadrupole photoionizing transitions, the amplitude is defined as:

$[T_{20}^{1\pm}]_{\nu=\pm\frac{1}{2}} =$

$$\sum_{\bar{k}\bar{m}} C_{l,M-\nu,1/2\nu}^{jM}\, Y_{lm-\nu}(\hat{n})\, \chi_\nu\, (-1)^{\bar{j}-\bar{m}} \begin{pmatrix} \bar{j} & 2 & j \\ -\bar{m} & 0 & m \end{pmatrix} \times D_{lj\to\bar{l}\,\bar{j}}\, (-1)^{\bar{j}+j+2} \tag{3.14}$$

An electric quadrupole transition from a $np_{1/2}$ initial state leads to the following ionization channels: $np_{1/2} \to \epsilon p_{3/2}, \epsilon f_{5/2}$, considering equation (3.14), we derived the following expressions for the $np_{1/2}$ ionization amplitudes:

$$[T_{20}^{1+}]_{np_{1/2}}^{m=1/2} = +\frac{1}{\sqrt{15}} Y_{10}\, D_{np_{1/2}\to\epsilon p_{3/2}} + \sqrt{\frac{3}{70}} Y_{30}\, D_{np_{1/2}\to\epsilon f_{5/2}} \tag{3.15}$$

$$[T_{20}^{1-}]_{np_{1/2}}^{m=1/2} = \frac{1}{\sqrt{30}} Y_{11}\, D_{np_{1/2}\to\epsilon p_{3/2}} - \sqrt{\frac{1}{35}} Y_{31}\, D_{np_{1/2}\to\epsilon f_{5/2}} \tag{3.16}$$

Each amplitude is linked to its specific photoelectron group delay, recognized as the Wigner time delay [42], and is defined as follows:

$$\eta = \tan^{-1}\frac{[Im\, T_{10}^{1\pm}]}{[Re\, T_{10}^{1\pm}]}, \qquad t = \frac{d\eta}{dE}. \tag{3.17}$$

Where η is the phase shift and t represents the Wigner time delay.

4 RESULTS AND DISCUSSION

4.1 Dipole and Quadrupole Contributions to Photoionization Time Delay in Atoms

The study of Wigner time delay in atomic photoionization provides information on the dynamics of atomic electrons in transition on the attosecond time scale, the time scale of atomic electron motion. This time delay generally has an angular dependence and calculations have been carried out looking at this angular dependence including only dipole transitions. Owing to angular momentum geometry, the amplitude for dipole photoionization vanishes at certain angles. Under such circumstances, the amplitude for quadrupole transitions dominates and can be studied; in particular, at angles where the dipole amplitude vanishes, the time delay exhibited is that of quadrupole photoionization, thereby allowing us to get information on the attosecond dynamics of quadrupole transitions. Fully relativistic calculations have been performed to delineate the circumstances under which the quadrupole channels dominate. Specifically, calculations have been carried out using relativistic random phase approximation (RRPA) for noble gas atoms for the angular distribution of time delay including both dipole and quadrupole channels where the transition from dipole-dominance to quadrupole-dominance is seen as a function of the angle between the photoelectron momentum and photon polarization.

4.1.1 Electric dipole transitions:

Here we focus on understanding the angular variations in photoemission time delay within the valence ns subshell of Argon (Ar). This analysis employs the dipole relativistic random phase approximation as a tool for studying the phenomenon. We examine electric dipole transitions that originate from initial $ns_{1/2}$ states. For an electric dipole transition from a ns initial state of a closed-shell atom we have:

$$ns_{1/2} \rightarrow \epsilon p_{1/2}, \epsilon p_{3/2} \tag{4.1}$$

Using Eq. (3.10), we derive the following expressions for the $ns_{1/2}$ ionization amplitude:

$$[\bar{T}_{10}^{1+}]_{ns_{1/2}}^{m=1/2} = -\frac{1}{3\sqrt{2}}\, Y_{10}\, D_{ns_{1/2}\rightarrow\epsilon p_{1/2}} - \frac{1}{3} Y_{10}\, D_{ns_{1/2}\rightarrow\epsilon p_{3/2}} \tag{4.2}$$

$$[\bar{T}_{10}^{1-}]_{ns_{1/2}}^{m=1/2} = \frac{1}{3} Y_{11}\, D_{ns_{1/2}\rightarrow\epsilon p_{1/2}} - \frac{1}{3\sqrt{2}} Y_{11}\, D_{ns_{1/2}\rightarrow\epsilon p_{3/2}} \tag{4.3}$$

Here we considered the linear polarization in the z direction M=0, polarization of the photoelectron as $\nu = \pm\frac{1}{2}$, and initial state magnetic quantum number as s=1/2, where $\lambda = 1, J = 1$.

4.1.2 Electric quadrupole transitions

Similarly, for an electric quadrupole transition from a $ns_{1/2}$ initial state of a closed-shell atom:

$$ns_{1/2} \rightarrow \epsilon d_{3/2}, \epsilon d_{5/2} \tag{4.4}$$

and the related reduced amplitudes are:

$$[\bar{T}_{20}^{1+}]_{ns_{1/2}}^{m=1/2} = -\frac{1}{5}\; Y_{20}\, D_{ns_{1/2}\rightarrow\epsilon d_{3/2}} - \frac{1}{5}\sqrt{\frac{3}{2}}\; Y_{20}\, D_{ns_{1/2}\rightarrow\epsilon d_{5/2}} \tag{4.5}$$

$$[\bar{T}_{20}^{1-}]_{ns_{1/2}}^{m=1/2} = \frac{1}{5}\sqrt{\frac{3}{2}}\; Y_{21}\, D_{ns_{1/2}\rightarrow\epsilon d_{3/2}} - \frac{1}{5}\; Y_{21}\, D_{ns_{1/2}\rightarrow\epsilon d_{5/2}} \tag{4.6}$$

Here we considered the linear polarization in the z direction M=0, polarization of the photoelectron as $\nu = \pm\frac{1}{2}$, and initial state magnetic quantum number as s=1/2, where $\lambda = 1, J = 2$.

4.2 Calculating the total Wigner time delay for Ar 3s

For each specific amplitude associated with the photoelectron transitions, the Wigner time delay is mathematically represented as $\tau = d\eta/dE$, where η denotes the phase uniquely associated with that particular amplitude. This concept captures the intricate relationship between the energy

variations and the corresponding phase shifts of the amplitude. When considering the total Wigner time delay for either the spin-up or spin-down states of the electron, a comprehensive perspective is obtained by evaluating the weighted average of the time delays originating from both the dipole and quadrupole components of the transition process. These weighting factors are intricately determined by the absolute squares of the respective amplitude values, creating a subtle interaction between the contributions from different transitions. One intriguing aspect to note is the pronounced dependence of these amplitudes on the angles of the photoelectron emission process. Given that the photoionization amplitudes inherently rely on the specific geometry of the atomic system and the orientation of the external fields, the angular dependency plays a pivotal role in shaping the resulting time delays. Since the amplitudes are angle-dependent, then so are the total Wigner time delay:

$$\tau_{ns_{1/2}} = \frac{\tau_{D,ns_{1/2}}^{m=1/2,+}\left|\left[T_{10}^{1+}\right]_{ns_{1/2}}^{m=1/2}\right|^2 + \tau_{Q,ns_{1/2}}^{m=\frac{1}{2},+}\left|\left[T_{20}^{1+}\right]_{ns_{1/2}}^{m=1/2}\right|^2}{\left|\left[T_{10}^{1+}\right]_{ns_{1/2}}^{m=1/2}\right|^2 + \left|\left[T_{20}^{1+}\right]_{ns_{1/2}}^{m=1/2}\right|^2} \tag{4.7}$$

where the subscripts D and Q refer to the dipole and quadrupole time delays, respectively. Note that the full T must be used for the weighting factors because the coefficients of the dipole and quadrupole amplitudes differ [23]. Due to the angular momentum geometry, certain angles result in the vanishing of the amplitude for dipole photoionization. In such cases, the amplitude for quadrupole transitions comes to the forefront, offering a fresh perspective on the dynamics at play. Specifically, where dipole amplitudes become negligible, the time delay becomes indicative of quadrupole photoionization, providing insights into attosecond dynamics within these transitions. Note that the dipole spin-up amplitude $[\bar{T}_{10}^{1+}]_{ns_{1/2}}^{m=1/2}$ vanishes at $\theta = 90^{\circ}$ so that the total spin-up time delay is entirely quadrupole there. Moreover, when considering the angle $\theta = 0^{\circ}$, it becomes apparent that despite the existence of a contribution from quadrupole transitions, its magnitude

remains notably smaller when compared to the influence of dipole transitions. Consequently, at this angle, $\theta = 0^{\circ}$, the total time delay is primarily governed by the effects of dipole interactions. The impact of quadrupole transitions at this specific angle is relatively minor, resulting in the time delay being predominantly characterized by the dominance of dipole interactions. Thus, it is expected that the total time delay should show considerable changes, as a function of θ in going from $\theta = 0^{\circ}$ to $\theta = 90^{\circ}$. To test these ideas, we have performed calculations on Ar 3s photoionization and the outcome of this calculation [44] is illustrated in Figure 4.1:

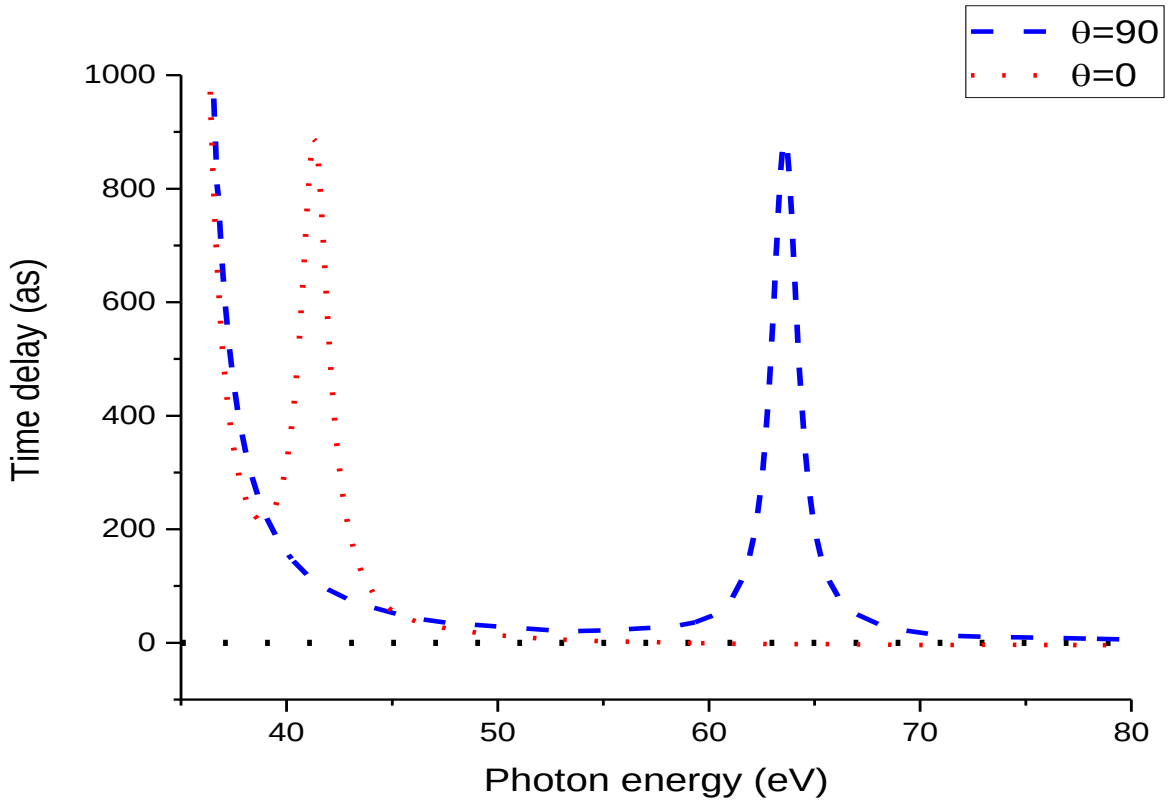

Figure 4-1 Total Wigner time delay for Ar 3s photoionization including both dipole and quadrupole channels at 0 and 90 degrees.

The data presented in Figure 4.1 indicates significant differences between the total Wigner spin-up time delay at 0 and 90 degrees. The time delay at θ=0° is primarily dipole, while the result at $\theta = 90^{\circ}$ is entirely quadrupole.

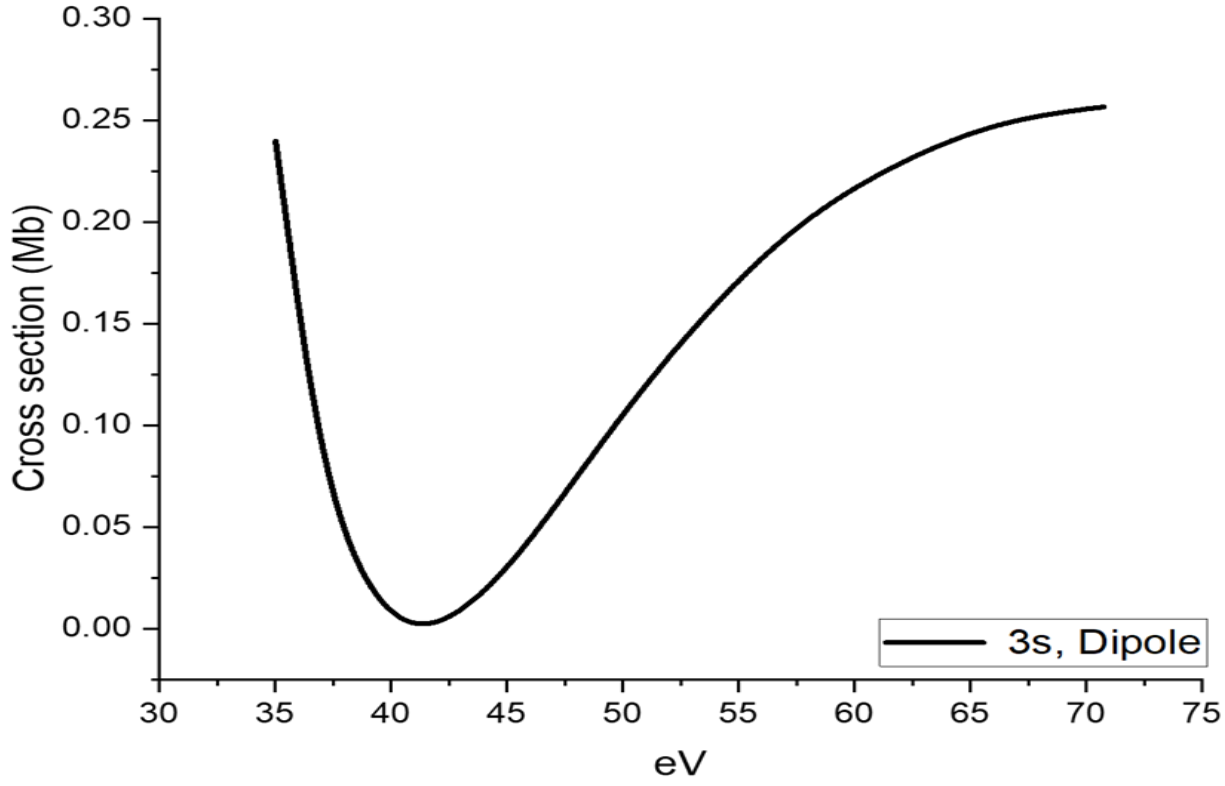

Figure 4-2 Ar 3s Photoionization Cross sections for dipole transitions vs. photon energy showing location for Cooper minimum.

It has been demonstrated that for the photoionization of ns subshells of closed-shell atoms by linearly polarized photons, the Wigner time delay at 90 degrees is solely due to quadrupole transitions. This causes the time delay to change significantly from dipole behavior, as illustrated by the example of Ar 3s photoionization. It was also discovered that quadruple transitions exhibited Cooper minima [51]. These findings provide a means of studying time delay in the quadrupole manifold.

4.3 Angular-Dependent Transition from Dipole to Quadrupole and Spin-Flip Dynamics

The interest in attosecond time delay (Wigner-Eisenberg-Smith, WES, time delay [1-3]) in atomic and molecular photoionization was stimulated by experimental measurements that captured time delay at the attosecond level [45, 46]. The interest was further heightened by the realization that studying attosecond time delay offers insights into atomic and molecular dynamics on a timescale aligned with the motion of electrons. This is particularly relevant to understanding how electrons behave during transitions from one quantum state to another. As a result, there has been a substantial number of both experimental and theoretical investigations focused on attosecond time delay in atomic and molecular photoionization, as documented in reference [47]. This research has predominantly centered around dipole transitions, which are the primary ways electrons move between states. Notably, one study noted the absence of "nondipole terms" contributing significantly to time delay [48]. More recent considerations have introduced non-dipole effects, albeit primarily at the nonrelativistic level and in lower-order analyses [49]. Additionally, most reported calculations have relied on nonrelativistic methodologies [50]. However, it's important to recognize that relativistic and non-dipole interactions can exert notable influence, particularly concerning angular distributions. The study of ns states within closed-shell atoms provides an effective platform to investigate this phenomenon. At the nonrelativistic dipole level, time delay manifests isotropically, irrespective of angle [49]. Importantly, even with the incorporation of relativistic effects at the dipole level, and when focusing on dominant transitions where the photoelectron's spin remains unchanged (no-spin-flip), the angular distribution retains its isotropic nature. However, the inclusion of spin-flip transitions, triggered by relativistic interactions, alongside non-dipole effects, disrupts the isotropy of the angular distribution, as elaborated upon. Consequently, measuring the angular distribution of time delay for these ns states

yields detailed insights into spin-flip and quadrupole-driven photoionization transitions. This type of information is typically challenging to gather without simultaneously detecting the photoelectron's spin and the orientation of the residual ion, in conjunction with the time delay. In the context of this report, the investigation centers on the photoionization of the 3s subshell of Argon (Ar), serving as a specific exemplar to elucidate the intricacies arising from the incorporation of spin-flip and quadrupole transitions. This case is particularly noteworthy due to the presence of the Cooper minimum [51] in the cross-sectional behavior, leading to pronounced time delays [52]. The photoionization time delay in the WES framework, measured in atomic units, for a complex transition amplitude T=|T|$e^{i\delta}$, is provided by:

$$t = \frac{d\ \arg[T(E)]}{dE} = \frac{d\delta}{dE} \tag{4.8}$$

In this context, E represents the energy of the emitted photoelectron. Our study relies on a powerful computational method called the relativistic-random-phase approximation (RRPA). This method helps us calculate transition matrix elements and their associated phases accurately. The RRPA is known for its ability to handle both relativistic effects and significant electron interactions, including dipole and quadrupole transitions. Specifically, the RRPA helps us determine the dipole transition matrix element for a transition from an initial state (n, κ) to a final state (E, $\bar{\kappa}$). This matrix element is a complex quantity:

$$D_{n\kappa\to \mathrm{E}\overline{k}} = i^{1-\bar{l}} e^{i\delta_{\overline{k}}} \left\langle E, \overline{\kappa} \middle\| Q_1^{(1)} \middle\| n, \kappa \right\rangle_{RRPA} \tag{4.9}$$

RRPA is a key factor that tells us about the dynamics of photoionization. The phase factor $\delta_{\overline{k}}$ brings in an energy-dependent aspect, telling us about the phase behavior of the final state wave function while considering how the electron behaves upon being ejected. Additionally, the phase $\delta(E)$, which describes the behavior of the electron's angular momentum (l) in the emitted photoelectron, is determined as follows:

$$\delta(E) = \tan^{-1}\{\frac{Im\langle E, \overline{\kappa}|\hat{d}|n, \kappa\rangle}{Re\langle E, \overline{\kappa}|\hat{d}|n, \kappa\rangle}\} \tag{4.10}$$

This equation provides insights into how the electron's angular momentum behaves during the photoionization process. It's important to note that similar principles apply when we consider quadrupole transitions. In these cases, the mathematics becomes even more complex, reflecting the intricate nature of higher-order interactions within atoms. The transition amplitudes, symbolized as T, are provided for the photoionization of ns states within a closed-shell atom when subjected to linearly polarized photons. These amplitudes pertain specifically to dipole transitions. To simplify the representation and focus on the aspects directly related to time delay, certain common factors that do not influence the time delay have been omitted from the equations:

$$\left[\overline{T}_{10}^{1+}\right]_{ns_{1/2}}^{m=1/2} = -\frac{1}{3\sqrt{2}} Y_{10} D_{ns_{1/2} \to \varepsilon p_{\frac{1}{2}}} - \frac{1}{3} Y_{10} D_{ns_{1/2} \to \varepsilon p_{3/2}} = \overline{T}_{10}^{1+} \tag{4.11}$$

$$\left[\overline{T}_{10}^{1-}\right]_{ns_{1/2}}^{m=1/2} = \frac{1}{3} Y_{11} D_{ns_{1/2} \to \varepsilon p_{1/2}} - \frac{1}{3\sqrt{2}} Y_{11} D_{ns_{1/2} \to \varepsilon p_{3/2}} = \overline{T}_{10}^{1-} \tag{4.12}$$

$\overline{T}_{10}^{1+}$ represents the No-spin-flip (NSF) and $\overline{T}_{10}^{1-}$ shows Spin-flip (SF) transitions. Similarly, for quadrupole transitions as:

$$\left[\overline{T}_{20}^{1+}\right]_{ns_{1/2}}^{m=1/2} = -\frac{1}{5} Y_{20} D_{ns_{1/2} \to \varepsilon d_{3/2}} - \frac{\sqrt{3}}{5\sqrt{2}} Y_{20} D_{ns_{1/2} \to \varepsilon d_{5/2}} = \overline{T}_{20}^{1+} \tag{4.13}$$

$$\left[\overline{T}_{20}^{1-}\right]_{ns_{1/2}}^{m=1/2} = \frac{\sqrt{3}}{5\sqrt{2}} Y_{21} D_{ns_{1/2} \to \varepsilon d_{3/2}} - \frac{1}{5} Y_{21} D_{ns_{1/2} \to \varepsilon d_{5/2}} = \overline{T}_{20}^{1-} \tag{4.14}$$

$\overline{T}_{20}^{1+}$ represents the No-spin-flip (NSF) and $\overline{T}_{20}^{1-}$ shows Spin-flip (SF) transitions. The notations + and – in this context distinguish between two types of transitions: non-spin-flip (+) and spin-flip (–) transitions, each characterized by distinct electron spin behaviors. When we consider both dipole and quadrupole transitions collectively, we can determine the complete amplitudes for both non-spin-flip and spin-flip processes. These amplitudes capture the combined effects of transitions

involving changes in electron spin, as well as the interactions associated with both dipole and quadrupole characteristics. Combining dipole and quadrupole transitions, the total non-spin-flip and spin flip amplitudes are given by:

$$\left[\overline{T}^{+}\right]_{ns_{1/2}}^{m=1/2} = \frac{\sqrt{2}}{\sqrt{3}}\left[\overline{T}_{10}^{1+}\right]_{ns_{1/2}}^{m=1/2} + \frac{\alpha h\nu}{\sqrt{30}}\left[\overline{T}_{20}^{1+}\right]_{ns_{1/2}}^{m=1/2} = \overline{T}^{+} \tag{4.15}$$

$$\left[\overline{T}^{-}\right]_{ns_{1/2}}^{m=1/2} = \frac{\sqrt{2}}{\sqrt{3}}\left[\overline{T}_{10}^{1-}\right]_{ns_{1/2}}^{m=1/2} + \frac{\alpha h\nu}{\sqrt{30}}\left[\overline{T}_{20}^{1}\right]_{ns_{1/2}}^{m=1/2} = \overline{T}^{-} \tag{4.16}$$

The symbol α, representing the fine structure constant, holds a numerical value of approximately 1/137. This constant plays a crucial role in quantum electrodynamics, characterizing the strength of the electromagnetic interaction between charged particles. In simpler terms, it quantifies the strength of electromagnetic forces in the atomic and subatomic world. On the other hand, $h\nu$ denotes the energy of a photon, measured in atomic units equivalent to approximately 27.21 electron volts (eV). We can calculate the time delays using Eq. (4.8), resulting in angle-dependent $\tau^{+}(\theta)$ and $\tau^{-}(\theta)$:

NSF time delay $$\tau^{+} = \frac{d}{dE}\arg\left[\overline{T}^{+}\right]_{ns_{1/2}}^{m=1/2} \tag{4.17}$$

SF time delay $$\tau^{-} = \frac{d}{dE}\arg\left[\overline{T}^{-}\right]_{ns_{1/2}}^{m=1/2} \tag{4.18}$$

NSF dipole time delay $$\tau_{dip}^{+} = \frac{d}{dE}\arg\left[\overline{T}_{10}^{1+}\right]_{ns_{1/2}}^{m=1/2} \tag{4.19}$$

The symbol θ in this context represents the angle between the direction in which the photoelectron is emitted and the polarization direction of the incident photon. This angle is crucial in understanding how the emitted electrons respond to the polarization of the incoming photons.

It's important to highlight that, theoretically, these angle-dependent time delays, $\tau^{+}(\theta)$ and $\tau^{-}(\theta)$, can be measured individually through a coincidence experiment. This experimental setup allows

for precise measurements of time delays corresponding to both no-spin-flip and spin-flip processes, providing valuable insights into the behavior of electrons during photoionization. However, in scenarios where coincidence measurements are not carried out, a total time delay is calculated by averaging over both no-spin-flip and spin-flip processes. This approach provides a comprehensive understanding of the overall time delay, considering the statistical distribution of electron emission angles and the contributions from various processes involved in photoionization. Where averaged total time delay is given by [51]:

$$\tau = \frac{\left|\overline{T}^{+}\right|^{2}\tau^{+}+\left|\overline{T}^{-}\right|^{2}\tau^{-}}{\left|\overline{T}^{+}\right|^{2}+\left|\overline{T}^{-}\right|^{2}} \tag{4.20}$$

A deep understanding can be gained by examining the angular momentum geometry associated with the various amplitudes involved in this context. It's essential to take note that typically, in the context of photoionization, the transition amplitude that predominantly occurs is denoted as $\left[\overline{T}_{10}^{1+}\right]_{ns_{1/2}}^{m=1/2}$. This amplitude is closely related to the spherical harmonic Y_{10}, a factor in the process. However, it's noteworthy that Y_{10} vanishes when the angle θ is set to 90 degrees, corresponding to a configuration where the emitted electron direction is perpendicular to the polarization direction of the incident photon. In practical terms, this means that at the θ =90 degree angle, the time delay τ is solely determined by the influence of quadrupole transitions. As a result, the overall time delay at this particular angle depends on the combined effects of quadrupole and spin-flip transitions. This is a significant observation as it highlights how the interplay between different types of transitions contributes to the overall time delay. The spin-flip (SF) amplitude, denoted as $\left[\overline{T}^{-}\right]_{ns_{1/2}}^{m=1/2}$, exhibits an interesting behavior: it vanishes completely at an emission angle of 0 degrees. This intriguing characteristic implies that any deviations from the non-spin-flip

(NSF) dipole time delay, represented as τ_{dip}^{+}, can solely be attributed to the influence of quadrupole transitions. In other words, when the emitted electron direction aligns perfectly with the photon polarization (0 degrees), the SF amplitude becomes negligible, emphasizing the significant role of quadrupole transitions in such scenarios. When considering the total time delay, denoted as τ, it is important to recognize that it represents a weighted average of both the NSF time delay (τ^{+}) and the SF time delay (τ^{-}). This weighted average is calculated across various energies and emission angles. Consequently, τ falls within the range defined by $\tau^{+}$and $\tau^{-}$for all energy levels and emission angles. This behavior is essential in understanding how the time delay varies across different conditions and highlights the relationship between NSF and SF time delays. Additionally, it's crucial to note that τ_{dip}^{+} is angle-independent, making it isotropic. This isotropic characteristic means that the NSF dipole time delay remains the same across all emission angles, providing a consistent reference point for analyzing deviations and variations caused by other transition types, such as quadrupole transitions.

The Ar 3s calculations were carried out using the RRPA method, as previously noted. In these calculations, all individual excitation and ionization channels were accounted, meaning that the correlations between these channels were incorporated into the final state of the system. All single excitation/ionization channels were included and coupled, i.e., interchannel coupling in the final state. An electric dipole transition from a np and ns initial states lead to the following ionization channels:

$$ns_{1/2} \rightarrow \varepsilon p_{1/2}, \varepsilon p_{3/2}; n = 1, 2, 3 \tag{4.21}$$

$$np_{1/2} \rightarrow \varepsilon s_{1/2}, \varepsilon d_{3/2}; n = 2, 3 \tag{4.22}$$

$$np_{3/2} \rightarrow \varepsilon s_{1/2}, \varepsilon d_{3/2}, \varepsilon d_{5/2}\,; n = 2, 3 \tag{4.23}$$

Which gives 16 dipole channels, and

$$ns_{1/2} \rightarrow \varepsilon d_{3/2}, \varepsilon d_{5/2}; n = 1, 2, 3 \quad (4.24)$$

$$np_{1/2} \rightarrow \varepsilon p_{3/2}, \varepsilon f_{3/2}; n = 2, 3 \quad (4.25)$$

$$np_{3/2} \rightarrow \varepsilon p_{1/2}, \varepsilon p_{3/2}, \varepsilon f_{5/2}, \varepsilon f_{7/2}\,; n = 2, 3 \quad (4.26)$$

Which gives 18 quadrupole channels. When we focus on low energy scenarios, it becomes evident that the 1s channels are essentially insignificant in both dipole and quadrupole situations. This means that, within the context of the specific energy range being examined, the behavior and contributions associated with the 1s channels can be disregarded or treated as negligible. In other words, these channels do not significantly impact the outcomes or results, whether we are dealing with dipole interactions or quadrupole interactions, due to their minimal relevance within the low-energy regime under consideration. In our calculations, we have determined that the photoionization cross section of Ar 3s displays a phenomenon known as a Cooper minimum. This occurs at a specific photon energy, which is approximately 41 eV as shown in Fig. 4.2.

In this context, the term "Cooper minimum" refers to a distinct feature in the cross section curve, where the probability of photoionization dips to a particularly low point at that specific energy level. This phenomenon is a notable characteristic of the photoionization behavior of the Argon atom's 3s electrons, and it provides valuable insights into their interaction with incident photons at this energy threshold [53]. The outcomes of our calculations pertaining to the WES time delay at an energy of 38 eV, which is proximate to but just below the Cooper minimum, have been presented in Figure 4.3. These results have been generated through four distinct levels of approximation. At the lowest approximation level, termed the "no-spin-flip dipole," denoted as τ_{dip}^{+}, as per Equation (4.19), it is observable that the time delay remains constant regardless of the angle considered. The value of this constant time delay is approximately 260 as. Remarkably, this

value closely resembles the outcome obtained from non-relativistic dipole calculations, as previously reported [35].

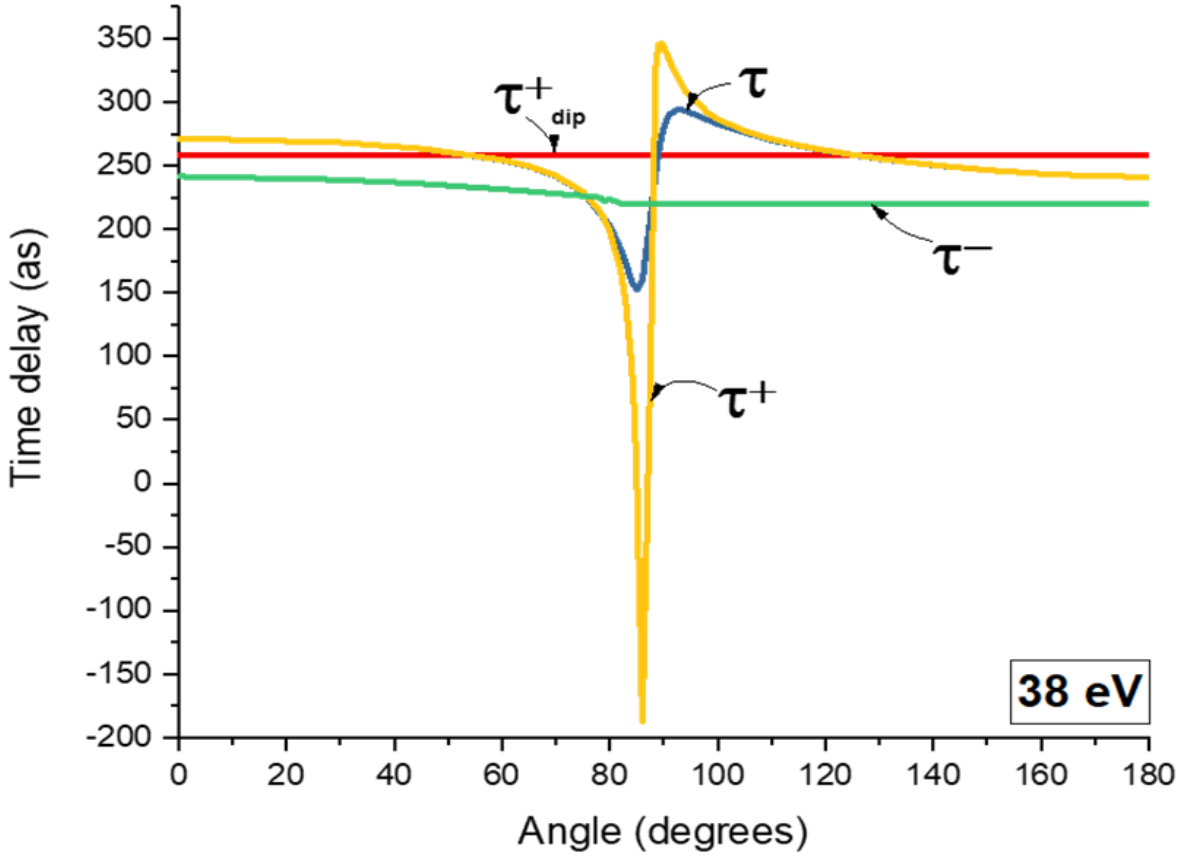

Figure 4-3 Calculated time delay for Ar 3s at 38 eV photon energy for linearly polarized photons as a function of angle with respect to photon polarization showing the total time delay, τ, the no-spin-flip (NSF) time delay, τ^+, the spin-flip (SF) time delay, τ^-, and the NSF dipole time delay, τ^+_{dip}.

The overall no-spin-flip time delay, denoted as τ^+ and accounting for quadrupole effects as described in Equation (4.17), presents a significantly contrasting pattern when compared to the previously mentioned dipole-only case. In this scenario, the time delay exhibits a pronounced angular dependence, with its values varying considerably as a function of the observation angle. Specifically, τ^+ demonstrates a substantial range of time delays, ranging from nearly -190 as to approximately 350 as. This results in a substantial change in time delay of more than 500 as over

a relatively narrow angular range. Notably, the most substantial deviations occur at an angle of approximately 90 degrees, which is perpendicular to the polarization direction of the incident photon. At this angle, the dipole contribution to τ^+vanishes. However, it is noteworthy that even at an angle of 0 degree, where the dipole contribution is still present, the quadrupole contribution remains evident, highlighting the significance of quadrupole effects in influencing the overall time delay behavior under these conditions. The disappearance of the quadrupole contribution at specific angles, often referred to as "magic angles" at approximately 57 and 123 degrees, explains why the values of the total τ^+ (no-spin-flip time delay) and τ^+_{dip} (the no-spin-flip dipole time delay) become equal at these particular angles. This equality is solely an outcome of the angular momentum geometry, emphasizing the geometric aspect of this phenomenon. When we examine the total spin-flip time delay, τ^-, as derived from Equation (4.18), it becomes evident that it exhibits a relatively weak angular dependence. It's important to note that, as indicated by the equations mentioned above, in the absence of the quadrupole contribution, τ^- would also be independent of the observation angle. Therefore, the weak angular dependence observed in τ^- is a consequence of the presence and influence of quadrupole interactions on this particular time delay. The behavior of the total time delay, denoted as τ(θ) and visually presented in Figure 4.3 while defined by Equation (4.20), closely mirrors that of τ^+except for a specific angular range spanning from 80 to 100 degrees. The reason for this deviation is primarily due to the magnitude of $\overline{T}^+$, which is much larger than $\overline{T}^-$outside this range. This discrepancy arises because $\overline{T}^+$is dominated by the dipole no-spin-flip transitions. However, the subtleties of angular momentum geometry come into play when we reach an observation angle of 90 degrees. At this specific angle, the dipole no-spin-flip amplitude, denoted as $\left[\overline{T}^{1+}_{10}\right]^{m=1/2}_{ns_{1/2}}$, vanishes. Consequently, the relative

significance of $\overline{T}^{-}$ becomes much more pronounced within this angular span. Given that τ(θ) represents a linear combination of both τ^{+} and τ^{-}, as described in Equation (4.20), its value naturally falls between the values of these two components. This relationship is visibly depicted in Figure 4.3. Furthermore, it's evident that within the angular range around 90 degrees, the magnitudes of the quadrupole no-spin-flip and dipole spin-flip amplitudes are quite comparable. This balance contributes to the relatively consistent behavior of the spin-flip time delay, τ^{-}, as a function of angle near 90 degrees. This, in turn, results in a total time delay, τ(θ), that varies over a somewhat narrower but still significant range, approximately spanning from 150 to 300 as, which corresponds to a difference of around 150 as when compared to τ^{+}. However, the overall pattern of the angular distribution in the total time delay, denoted as τ(θ), closely resembles that of the no-spin-flip time delay τ^{+}, albeit with a substantial truncation. In any case, it is evident that the incorporation of relativistic spin-flip and quadrupole effects results in a significant alteration of the angular dependence observed in the WES time delay. At a photon energy of 40 eV, which is closer to the Cooper minimum, the dynamics of photoionization exhibit notably different quantitative behaviors, despite a relatively minor change of only 2 eV in photon energy. Specifically, the no-spin-flip time delay, denoted as τ^{+}, experiences a remarkable drop from approximately 300 as to almost -1000 as within the angular region around 90 degrees. Simultaneously, the total time delay, τ, undergoes a significant reduction of around 300 as within this angular zone. This disparity in behavior can be attributed to the varying energy dependencies of spin-flip (SF) and quadrupole transitions. Essentially, these transitions respond differently to changes in photon energy, resulting in the observed differences in time delay dynamics at this particular photon energy of 40 eV. This situation is depicted in Figure 4.4, where it becomes evident that the effects of spin-flip and quadrupole transitions are quite significant. However, the

detailed shapes of these effects differ from the previous case. At 40 eV, being closer to the Cooper minimum, the dynamics take on a somewhat different character. Due to angular momentum geometry, τ^{+}_{dip} exhibits isotropic behavior and is relatively large in terms of time delays

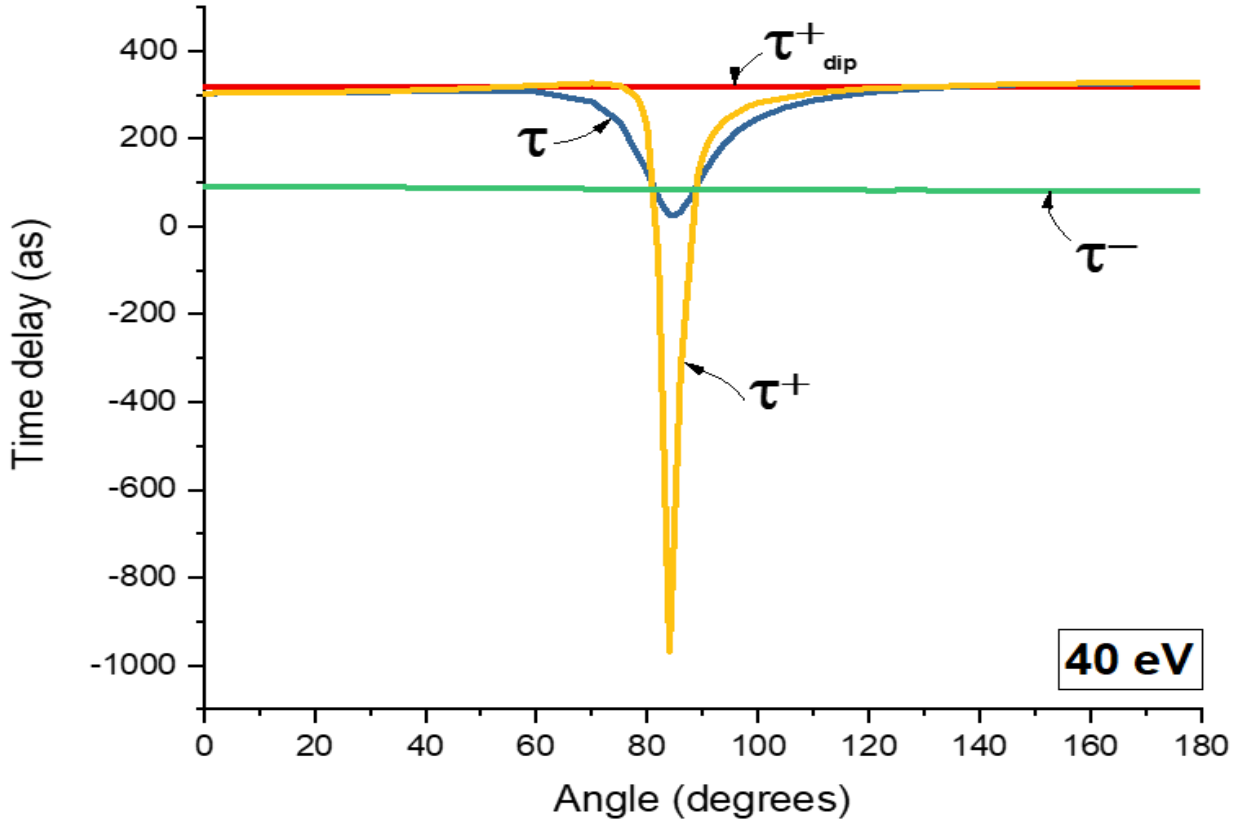

Figure 4-4 Calculated time delay for Ar 3s at 40 eV photon energy for linearly polarized photons as a function of angle with respect to photon polarization showing the total time delay, τ, the no-spin-flip (NSF) time delay, τ^{+}, the spin-flip (SF) time delay, τ^{-}, and the NSF dipole time delay, τ^{+}_{dip}.

exceeding 300 as. Additionally, τ^{+} undergoes a substantial traverse within the 90-degree region, transitioning from approximately 300 as to almost -1000 as over a small angular range. This dramatic variation is primarily driven by the presence of quadrupole transitions. Furthermore, the shape of this time delay is distinctly different, reflecting the unique dynamics associated with this photon energy. In contrast, the spin-flip time delay, τ^{-}, is essentially isotropic at this energy

because the contribution from quadrupole transitions is much smaller compared to the dipole transitions. This situation contrasts with the scenario at 38 eV, where a weak angular dependence of τ^- is observed. Once again, the total time delay exhibits a shape similar to that of τ^+ but is significantly truncated. However, it still experiences a substantial variation of approximately 300 as within the 90-degree region. This detailed analysis underscores the extreme sensitivity of the angular dependence of time delay to the underlying dynamics, emphasizing that even slight changes in photon energy can lead to dramatic variations in these behaviors. As we transition away from the vicinity of the Cooper minimum, we can observe the behavior of time delay at photon energies of 90.07 eV and 120 eV, which is presented in Figure 4.5. Notably, there is a substantial reduction in the overall scale of the time delay when compared to the energies closer to the Cooper minimum. Moreover, in this representation, we focus on a limited range of angles. This is because, at these higher energies, the spin-flip and quadrupole channels only induce significant angular dependence within a specific angular span, typically around 90 degrees. One noteworthy observation is that the value of τ_{dip}^+remains relatively stable as we transition from one energy to the other. However, the detailed dynamics of the time delay exhibit marked differences. This contrast is manifested in the rather asymmetric shape of τ^+ and, consequently, τ as they vary with angle for the lower energy, while displaying a symmetric shape for the higher energy. In essence, this analysis underscores the complex and energy-dependent nature of time delay behavior, highlighting how changes in photon energy can lead to distinct patterns in the angular dependence of these parameters. At 120 eV, significantly distant from the Cooper minimum, two noteworthy distinctions become apparent when compared to lower-energy scenarios. Firstly, the entire scale of time delay is substantially reduced. In other words, the time delays observed at this higher energy level are much smaller in magnitude compared to those at lower energies. This implies that

the time taken for various photoionization processes to occur is significantly shorter. Secondly, the influence of spin-flip (SF) and quadrupole transitions, although still notable in percentage terms, becomes significant primarily within a limited angular range around 90 degrees. In other words, the angular dependence of time delay is most pronounced in the vicinity of 90 degrees, while the effects of SF and quadrupole transitions become less pronounced at other angles. When considering energies at different points away from the Cooper minimum, there is a consistent pattern: significant changes in time delay are always observed within the 90-degree region. However, the specific details of these changes vary due to the energy-dependent dynamics of the photoionization process. In essence, these observations highlight how the behavior of time delay is influenced by both energy levels and angular factors, emphasizing the intricate nature of photoionization dynamics. The evolution of the angular dependence of the total time delay, τ, as it relates to various photon energies, provides a fascinating insight into how this parameter changes both in magnitude and shape across the energy spectrum, particularly as we move away from the Cooper minimum region.

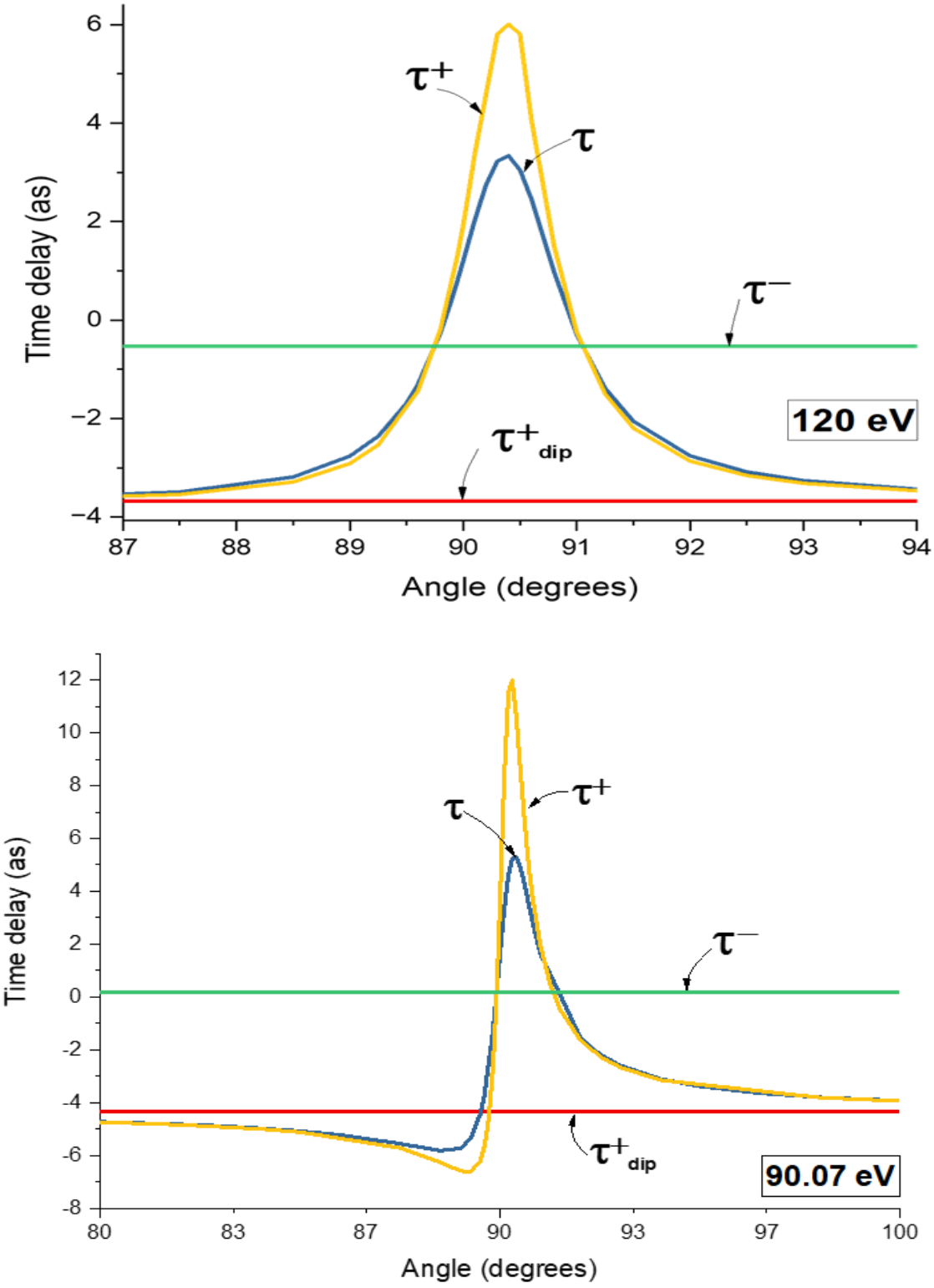

Figure 4-5 As Fig. 4.3 except for photon energy 90.07 eV (upper plot) and 120 eV (lower plot).

To gain a deeper understanding of how τ evolves concerning both energy and angle, let's turn our attention to Figure 4.6. Here, we examine a range of photon energies spanning from 38 eV to 269.9 eV. This comprehensive exploration reveals that the characteristics of time delay undergo substantial transformations in response to variations in energy. These transformations are a direct consequence of the distinct dynamics associated with each energy level. One striking observation is the marked reduction in the overall magnitude of time delays as we ascend to higher energies beyond the Cooper minimum region. Alongside this decrease in magnitude, the angular distributions of time delays also undergo significant alterations, illustrating the dynamic nature of these phenomena. In the vicinity of the Cooper minimum region, as vividly portrayed in Figure 4.6, a pronounced angular dependence of time delay unfolds across the entire angular span, ranging from 0 to 180 degrees. This robust angular dependence is a direct consequence of the unique dynamics that govern the Cooper minimum region. Here, the amplitude $\left[\overline{T}_{10}^{1+}\right]_{ns_{1/2}}^{m=1/2}$ is relatively small, amplifying the relative significance of contributions from

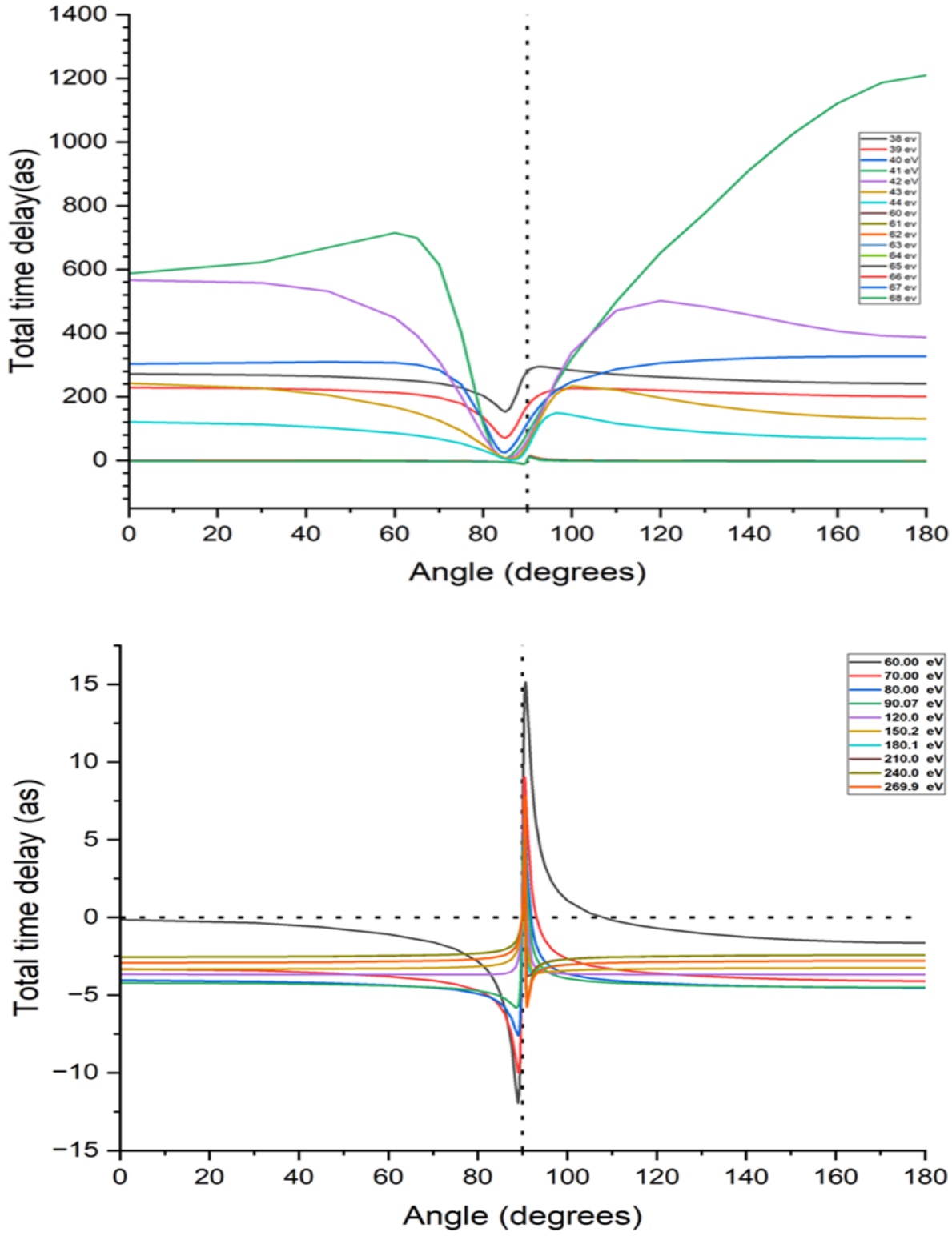

Figure 4-6 Total time delay, τ, for a variety of energies as functions of the angle. Note the differing vertical scales on the upper and lower plots.

quadrupole and spin-flip transitions. Consequently, these contributions exert their influence broadly across the entire angular range, as is evident from the figure. However, as we advance to higher photon energies, this intricate pattern undergoes a transformation. In these instances, the behavior of time delay is no longer governed by the dynamics near the Cooper minimum, leading to a notably different scenario. Instead, the angular dependence of time delay becomes most pronounced in the vicinity of 90 degrees. This peculiar behavior arises because, due to angular momentum considerations, the amplitude $\left[\overline{T}_{10}^{1+}\right]_{ns_{1/2}}^{m=1/2}$ vanishes around the 90-degree mark. Consequently, it is precisely at these angles that the contributions from quadrupole and spin-flip transitions exert their most substantial influence. Beyond this specific angular region, the time delay closely aligns with τ_{dip}^{+}, resulting in a relatively flat angular distribution.

5 CONCLUSION

Using the advanced fully relativistic RRPA methodology, we conducted comprehensive calculations on the photoionization cross sections of the ground states of the superheavy element Og (Z = 118), a closed subshell system. Our analysis revealed intriguing patterns: the dominant 5f and 4f subshells, along with the 6d subshells near the thresholds, played a pivotal role in shaping the total photoionization cross sections across a wide range of photon energies. A striking observation was the mirroring effect displayed by weaker subshells in regions where a specific subshell exerted dominance, underscoring the significant influence of interchannel coupling. Notably, the substantial spin–orbit splitting led to distinct dynamics within inner-shell spin–orbit doublets. In Og, both 5f levels fell between the $6p_{1/2}$ and $6p_{3/2}$ levels, highlighting the profound impact of relativistic interactions in high-Z atoms. It is crucial to emphasize that Og, despite its uniqueness as a superheavy element, exhibited behavior typical of closed subshell systems within the periodic table. Consequently, our findings strongly suggest that analogous interchannel coupling effects in photoionization are likely to prevail across all superheavy elements. In essence, the insights detailed in this report are anticipated to have broad applicability, providing a foundational understanding of the underlying phenomenology.

Our exploration extended deeper into the domain of attosecond time delay, probing the intricacies of time delay calculations. The study of attosecond time delay offers a window into the dynamic world of atomic and molecular behavior at the timescale of electron motion during transitions between states. Our goal was to integrate both dipole and quadrupole transitions, aiming to capture a comprehensive angular distribution of time delay. Typically, dipole transitions exhibit larger cross sections and amplitudes compared to quadrupole transitions. However, within dipole transitions, there are specific points of vanishing amplitudes where quadrupole transitions come

into play. Our fully relativistic exploration of the angular distribution of WES time delay, originating from the photoionization of ns states in closed-shell atoms under linearly polarized electromagnetic radiation, revealed a complex pattern influenced by dynamic interactions and angular momentum geometry. At a 90-degrees angle, perpendicular to the photon polarization, the total time delay, averaged across both no-spin-flip and spin-flip transitions, was predominantly or entirely governed by quadrupole and spin-flip transitions. This phenomenon was markedly pronounced in the case of Ar 3s, especially in the energy range associated with the Cooper minimum. It is important to mention that investigating no-spin-flip time delay effects, despite their greater significance, can be challenging due to experimental limitations. Coincidence experiments are required in order to overcome these challenges. It is noteworthy that at the nonrelativistic dipole level, the WES time delay exhibits isotropy; hence, any angular variations indicate the presence of relativistic and/or quadrupole interactions. Studying the angular distribution of time delay around the 90-degrees region provides crucial insights into spin-flip and quadrupole transitions at the attosecond scale, which aligns with the natural timescale of atomic and molecular electron motion. These findings are not specific to particular elements but rather hold true for ns subshells of any closed-shell atom. We are currently extending our investigations to explore additional scenarios. Furthermore, we are exploring the potential wealth of information that can be gleaned through the use of circularly polarized light.

REFERENCES

[1]: Pershina, V., and B. Fricke. "Relativistic effects in physics and chemistry of element 105. IV. Their influence on the electronic structure and related properties." The Journal of chemical physics 99.12 (1993): 9720-9729.

[2]: Grant, I. P., B. J. McKenzie, P. H. Norrington, D. F. Mayers, and N. C. Pyper. "Atomic multiconfigurational Dirac-Fock package." Comput. Phys. Commun.;(Netherlands) 21, no. 2 (1980).

[3]: Grant, Ian P., ed. Relativistic quantum theory of atoms and molecules: theory and computation. New York, NY: Springer New York, 2007.

[4]: Derevianko, A., W. R. Johnson, and K. T. Cheng. "Non-dipole effects in photoelectron angular distributions for rare gas atoms." Atomic Data and Nuclear Data Tables 73.2 (1999): 153-211.

[5]: Schultze, Martin, Markus Fieß, Nicholas Karpowicz, Justin Gagnon, Michael Korbman, Michael Hofstetter, S. Neppl et al. "Delay in photoemission." science 328, no. 5986 (2010): 1658-1662.

[6]: Holzmeier, Fabian, Jennifer Joseph, Jean-Christophe Houver, Mogens Lebech, Danielle Dowek, and Robert R. Lucchese. "Influence of shape resonances on the angular dependence of molecular photoionization delays." Nature communications 12, no. 1 (2021): 7343.

[7]: Guenot, Diego, Kathrin Klünder, C. L. Arnold, David Kroon, J. Marcus Dahlström, Miguel Miranda, Thomas Fordell et al. "Photoemission-time-delay measurements and calculations close to the 3 s-ionization-cross-section minimum in ar." Physical Review A 85, no. 5 (2012): 053424.

[8]: Klünder, Kathrin, J. M. Dahlström, Mathieu Gisselbrecht, Thomas Fordell, Marko Swoboda, Diego Guenot, Per Johnsson et al. "Probing single-photon ionization on the attosecond time scale." Physical Review Letters 106, no. 14 (2011): 143002.

[9]: Elghazawy, Karim I., and Chris H. Greene. "Wigner Time Delay in Photoionization: A 1D Model Study." arXiv preprint arXiv:2305.07215 (2023).

[10]: Kheifets, Anatoli S., Daniele Toffoli, and Piero Decleva. "Angular dependent time delay near correlation induced Cooper minima." Journal of Physics B: Atomic, Molecular and Optical Physics 53.11 (2020): 115201.

[11]: Harrison, George R. "Series limit absorption in sodium vapor." Physical Review 24, no. 5 (1924): 466.

[12]: Samson, James AR. "Photoionization of atoms and molecules." Physics Reports 28.4 (1976): 303-354.

[13]: Manson, Steven T. "Atomic photoelectron spectroscopy, part I." Advances in electronics and electron physics. Vol. 41. Academic Press, 1976. 73-111.

[14]: Starace, Anthony F. "Theory of atomic photoionization." Handbuch der Physik 6 (1982): 1-121.

[15]: Power, Edwin Albert, and Sigurd Zienau. "Coulomb gauge in non-relativistic quantum electro-dynamics and the shape of spectral lines." Philosophical Transactions of the Royal Society of London. Series A, Mathematical and Physical Sciences 251.999 (1959): 427-454.

[16]: J. J. Sakurai, Advanced Quantum Mechanics (AddisonWesley, Reading, 1967), p. 39.

[17]: Boßmann, Lea. On the Dipole Approximation. Diss. Master Thesis, University of Munich, 2016.

[18]: Martins, J. B. (2021). Dynamique électronique dans les molécules organiques par la spectroscopie Core-Hole Clock (Doctoral dissertation, Sorbonne Université).

[19]: Manson, Steven T. "The Spin-Orbit Interaction: A Small Force with Large Implications." Atoms 11.6 (2023): 90.

[20]: Ron, Akiva, I. B. Goldberg, J. Stein, Steven T. Manson, R. H. Pratt, and R. Y. Yin. "Relativistic, retardation, and multipole effects in photoionization cross sections: Z, n, and l dependence." Physical Review A 50, no. 2 (1994): 1312.

[21]: Ong, Warren, and S. T. Manson. "The photoelectron angular distribution of xenon 5s." Journal of Physics B: Atomic and Molecular Physics 11.3 (1978): L65.

[22]: Ren, Xinguo, Patrick Rinke, Christian Joas, and Matthias Scheffler. "Random-phase approximation and its applications in computational chemistry and materials science." Journal of Materials Science 47 (2012): 7447-7471.

[23]: Johnson, W. R., and C. D. Lin. "Multichannel relativistic random-phase approximation for the photoionization of atoms." Physical Review *A* 20.3 (1979): 964.

[24]: Munasinghe, Chathuranga Rasadi. "Relativistic and Interchannel Effects on Branching Ratios of Spin-Orbit Doublets." (2021).

[25]: Johnson, W. R., C. D. Lin, K. T. Cheng, and C. M. Lee. "Relativistic random-phase approximation." Physica Scripta 21, no. 3-4 (1980): 409.

[26]: Walker, T. E. H., and J. T. Waber. "Spin-orbit coupling photoionization." Journal of Physics B: Atomic and Molecular Physics 7.6 (1974): 674.

[27]: Manson, Steven T., and Anthony F. Starace. "Photoelectron angular distributions: energy dependence for s subshells." Reviews of Modern Physics 54.2 (1982): 389.

[28]: Razavi, A. K., Hosseini, R. K., Keating, D. A., Deshmukh, P. C., & Manson, S. T. (2020). Photoionization of superheavy atoms: correlation and relativistic effects. Journal of Physics B: Atomic, Molecular and Optical Physics, *53*(20), 205203.

[29]: L. Eisenbud, Ph. D. thesis, Princeton University (1948)

[30]: Kheifets, A. S., and I. A. Ivanov. "Delay in atomic photoionization." Physical review letters 105.23 (2010): 233002.

[31]: Eckle, P., A. N. Pfeiffer, C. Cirelli, A. Staudte, R. Dorner, H. G. Muller, M. Buttiker, and U. Keller. "Attosecond ionization and tunneling delay time measurements in helium." science 322, no. 5907 (2008): 1525-1529.

[32]: Pazourek, Renate, Stefan Nagele, and Joachim Burgdörfer. "Attosecond chronoscopy of photoemission." Reviews of Modern Physics 87.3 (2015): 765.

[33]: Schultze, Martin, Krupa Ramasesha, C. D. Pemmaraju, S. A. Sato, D. Whitmore, A. Gandman, James S. Prell et al. "Attosecond band-gap dynamics in silicon." Science 346, no. 6215 (2014): 1348-1352.

[34]: Haessler, Stefan, J. Caillat, W. Boutu, C. Giovanetti-Teixeira, T. Ruchon, T. Auguste, Z. Diveki et al. "Attosecond imaging of molecular electronic wavepackets." Nature Physics 6, no. 3 (2010): 200-206.

[35]: Saha, S., Mandal, A., Jose, J., Varma, H. R., Deshmukh, P. C., Kheifets, A. S., ... & Manson, S. T. (2014). Relativistic effects in photoionization time delay near the Cooper minimum of noble-gas atoms. Physical Review A, 90(5), 053406.

[36]: Baltuška, A., Udem, T., Uiberacker, M., Hentschel, M., Goulielmakis, E., Gohle, C., ... & Krausz, F. (2003). Attosecond control of electronic processes by intense light fields. Nature, 421(6923), 611-615.

[37]: Eckle, P., Smolarski, M., Schlup, P. et al. Attosecond angular streaking. Nature Phys 4, 565–570 (2008).

[38]: Klünder, K., Dahlström, J. M., Gisselbrecht, M., Fordell, T., Swoboda, M., Guenot, D., ... & L'Huillier, A. (2011). Probing single-photon ionization on the attosecond time scale. Physical Review Letters, 106(14), 143002.

[39]: Smith, F. T. (1960). Lifetime matrix in collision theory. Physical Review, 118(1), 349.

[40]: Gustafson, K., & Sinha, K. (1980). On the Eisenbud-Wigner formula for time-delay. Letters in Mathematical Physics, 4, 381-385.

[41]: Wigner, E. P. (1955). Lower limit for the energy derivative of the scattering phase shift. Physical Review, 98(1), 145.

[42]: Kheifets, A., Mandal, A., Deshmukh, P. C., Dolmatov, V. K., Keating, D. A., & Manson, S. T. (2016). Relativistic calculations of angle-dependent photoemission time delay. Physical Review *A*, *94*(1), 013423.

[43]: Anatoli S Kheifets 2023 J. Phys. B: At. Mol. Opt. Phys. 56 022001.

[44]: Hosseini, Rezvan, Steven Manson, and Pranawa Deshmukh. "Angular Dependence of the Transition from Dipole to Quadrupole Photoionization Time Delay in Atoms." APS Division of Atomic, Molecular and Optical Physics Meeting Abstracts. Vol. 2022. 2022.

[45]: Schultze, M., Fieß, M., Karpowicz, N., Gagnon, J., Korbman, M., Hofstetter, M., ... & Yakovlev, V. S. (2010). Delay in photoemission. science, 328(5986), 1658-1662.

[46]: Klünder, K., Dahlström, J. M., Gisselbrecht, M., Fordell, T., Swoboda, M., Guenot, D., ... & L'Huillier, A. (2011). Probing single-photon ionization on the attosecond time scale. Physical Review Letters, 106(14), 143002.

[47]: F. Holzmeier, J. Joseph, J. C. Houver, M. Lebech, D. Dowek and R. R. Lucchese, Influence of shape resonances on the angular dependence of molecular photoionization delays, Nat. Commun. 12, 7343 (2021).

[48]: Śpiewanowski, M. D., & Madsen, L. B. (2012). Nondipole effects in attosecond photoelectron streaking. Physical Review A, 86(4), 045401.

[49]: Amusia, M. Y., & Chernysheva, L. V. (2020). Nondipole Effects in Time Delay of Photoelectrons from Atoms, Negative Ions, and Endohedrals. JETP Letters, 112, 673-679.

[50]: Deshmukh, P. C., Banerjee, S., Mandal, A., & Manson, S. T. (2021). Eisenbud–Wigner–Smith time delay in atom–laser interactions. The European Physical Journal Special Topics, 1-14.

[51]: J. W. Cooper, Photoionization from Outer Atomic Subshells. A Model Study, Phys. Rev. 128, 681-693 (1962).

[52]: D. Guénot, K. Klunder, C. L. Arnold, D. Kroon, J. M. Dahlström, M. Miranda, T. Fordell, M. Gisselbrecht, P. Johnsson, J. Mauritsson, E. Lindroth, A. Maquet, R. Taïeb, A. L'Huillier, and A. S. Kheifets, Photoemission-time-delay measurements and calculations close to the 3s-ionization-cross-section minimum in Ar, Phys. Rev. A 85, 053424 (2012).

[53]: Kheifets, A. S., Toffoli, D., & Decleva, P. (2020). Angular dependent time delay near correlation induced Cooper minima. Journal of Physics B: Atomic, Molecular and Optical Physics, 53(11), 115201.

[54]: Hammerland, D., P. Zhang, A. Bray, C. F. Perry, S. Kuehn, P. Jojart, I. Seres et al. "Effect of electron correlations on attosecond photoionization delays in the vicinity of the Cooper minima of argon." arXiv preprint arXiv:1907.01219 (2019).

[55]: E.P. Wigner, Phys. Rev. 98, 145 (1955).

[56]: F.T. Smith, Phys. Rev. 118, 349 (1960).

[57]: Ditchburn, Robert William, J. Tunstead, and J. G. Yates. "The continuous absorption of light in potassium vapour." Proceedings of the Royal Society of London. Series A. Mathematical and Physical Sciences 181, no. 987 (1943): 386-399.

[58]: Beterov, I. I., C. W. Mansell, E. A. Yakshina, I. I. Ryabtsev, D. B. Tretyakov, V. M. Entin, C. MacCormick, M. J. Piotrowicz, A. Kowalczyk, and S. Bergamini. "Cooper minima in the transitions from low-excited and Rydberg states of alkali-metal atoms." arXiv preprint arXiv:1207.3626 (2012).

[59]: Banerjee, Sourav, Pranawa C. Deshmukh, Anatoli S. Kheifets, and Steven T. Manson. "Effects of spin-orbit-interaction-activated interchannel coupling on photoemission time delay." Physical Review A 101, no. 4 (2020): 043411.

[60]: Jose, Jobin, S. Baral, Pranawa C. Deshmukh, and Steven T. Manson. "Relativistic and correlation effects in the photoionization dynamics of oganesson (Z= 118): Spin-orbit-interaction-activated interchannel coupling effects." Physical Review A 102, no. 2 (2020): 022813.

[60]: Keating, David A. "Evolution of Relativistic Effects in the Photoionization of Free and Confined Heavy Atoms." (2018).

APPENDICES

Appendix A

Cooper minimum:

Cooper minima are well-established phenomena in photoionization cross sections, occurs a Cooper minimum materializes at an energy level where the dipole matrix element's positive and negative contributions cancel each other out due to the overlap between the initial and final state wave functions. This convergence results in a zero value for the matrix element as a function of energy [19]. Both theoretical and experimental studies have identified numerous instances of these minima in the ground states of atoms [58]. Notably, as the atomic number increases, the wave function becomes more compact for a given nl state, causing the Cooper minimum to shift closer to the threshold, resulting in lower photoelectron energies. The observation of Cooper minima in photoionization cross-sections and discrete spectrum transition probabilities provides valuable insights into the electronic structure of atoms. These minima were initially discovered experimentally [57] and later explained by Cooper [51].

Appendix B

SOIAIC:

This phenomenon known as spin-orbit-interaction activated interchannel coupling (SOIAIC) refers to the interchannel coupling between photoionization channels originating from spin-orbit split subshells. This effect is exclusively driven by relativistic forces, particularly the spin-orbit interaction [59]. Unlike in low-Z atoms, the spin-orbit splitting in superheavy elements is notably pronounced due to the heightened influence of relativistic effects. SOIAIC serves as a compelling illustration of many-body interactions, showcasing the interchannel coupling among

various photoemission channels originating from the two states that form a spin-orbit doublet. This phenomenon sheds light on the complex dynamics within high-Z atoms, providing crucial information into the behavior of electrons in these elements [60]. The enhanced spin-orbit splitting in superheavy elements intensifies the significance of SOIAIC, offering a unique perspective into the interchannel coupling phenomena in the realm of relativistic quantum mechanics.